

On the role of bottom roughness in overflows

Tamay M. Özgökmen^{a,*}, Paul F. Fischer^b

^a *RSMAS/MPO, University of Miami, Miami, FL, United States*

^b *Mathematics and Computer Science Division, Argonne National Laboratory, Argonne, IL, United States*

Received 1 July 2007; received in revised form 18 October 2007; accepted 18 October 2007

Available online 4 November 2007

Abstract

Overflows play an important role in the downwelling limb of the oceanic thermohaline circulation. In light of the recognition that some overflows are not homogenous but exhibit a vertical density structure, and details of topography influence the pathways of some overflows, the impact of topographic roughness on the product property distribution is explored using the 3D non-hydrostatic spectral element model Nek5000. Numerical experiments are carried out by varying bottom roughness amplitude and ambient stratification parameters, in a regime where equilibrated product water masses are formed in a non-rotating environment.

Our main finding is that bottom roughness can influence the overflow product distribution such that the highest salinity classes are removed and neutral buoyancy level is attained higher up in the stratified ambient water column. It is also shown that the form drag coefficients in overflows over rough bottom can be much larger than the skin drag coefficient over smooth bottom. To our knowledge, form drag has never been measured in oceanic overflows. As such, these numerical experiments imply that such measurements would be useful for a better understanding of overflow dynamics. It is also found that the ratio of source and product overflow mass transports is robust to changes in bottom roughness. This appears to happen because the distribution of entrainment is totally different in the case of rough bottom. Entrainment tends to initiate earlier (due to vertical motion induced by topography) and terminate earlier (due to development of form drag) than that over smooth topography.

© 2007 Elsevier Ltd. All rights reserved.

1. Introduction

The thermohaline circulation in the ocean can be broadly divided into three components. The first component is the deep-water mass formation, or downwelling. It is generally accepted that deep-water mass formation takes place in polar and marginal seas by convection (Spall and Pickard, 2001). The resulting dense water masses are introduced into the circulation via localized processes, such as overflows (Price and Baringer, 1994) that feed the bottom (e.g., Antarctic Bottom Water) and deep (e.g., North Atlantic Deep Water) water masses in the ocean. The second component is the transport of these water masses inside the various basins, not only through large-scale gyres, jets and meso-scale eddies, but also by flows through gaps and passages as some of

* Corresponding author.

E-mail address: tozgokmen@rsmas.miami.edu (T.M. Özgökmen).

the dense flows are in direct contact with bottom topography (Schmitz, 1995). The third component is the upwelling of bottom and deep water masses to complete the circulation.

Prediction of the Earth's future climate conditions necessarily relies on the accuracy of global circulation models, and it is known that numerical simulation of the ocean's thermohaline circulation is a central problem regarding this task. Thus, ocean general circulation models (OGCMs) must be constantly improved to capture these three components as realistically as possible. Clearly, ocean observations are critical to achieve this objective. The main challenge regarding observations is the large separation of scales in the ocean, or more formally the high Reynolds number $Re = UL/\nu$. Using a characteristic speed scale $U \approx 10^{-1} \text{ m s}^{-1}$, horizontal length scale $L \approx 10^5 \text{ m}$ and kinematic viscosity $\nu = 10^{-6} \text{ m}^2 \text{ s}^{-1}$, an upper limit can be obtained as $Re \approx 10^{10}$. Since the number of degrees of freedom in the case of homogenous, isotropic turbulence is $\sim Re^{9/4}$ (Lesieur, 1997), we obtain $\approx O(10^{22})$ as an upper limit for the needed spatial sampling points, at a given time. Therefore, it is difficult at the present time to collect observations describing the state of the oceanic velocity and tracer fields in all spatial and temporal coordinates. The sampling problem is particularly pronounced regarding the observation of the upwelling limb of the thermohaline circulation in that it is not clearly known neither by which mechanisms this takes place (Munk and Wunsch, 1998; Wunsch and Ferrari, 2004), nor exactly where the upwelling takes place. Ocean observations point to the role played by rough topography of the oceanic ridges (Poltzin et al., 1997; Ferron et al., 1998; Ledwell et al., 2000), isolated topographic obstacles such as seamounts (Nabatov and Ozmidov, 1988; Gibson et al., 1993; Lueck and Mudge, 1997; Kunze and Toole, 1997; Lavelle et al., 2004), mixing over the continental slope (Moum et al., 2002), and inside the canyons of mid-ocean ridges (Thurnherr and Speer, 2003; Thurnherr et al., 2004; Thurnherr, 2006). Given the large number of such topographic features, upwelling appears to be widely distributed in space, and further observations are needed to map the spatial and temporal distribution of ocean upwelling.

Regarding the downwelling limb of the thermohaline circulation, both the observation and modeling of the deep-convection process remain challenging due to the small spatial and temporal scales of mixed patches (Marshall and Schott, 1999). Nevertheless, the state of knowledge is significantly better than the upwelling limb of the thermohaline circulation, because most of the deep and intermediate water masses are released into the general circulation from a few main overflows, namely those from the Mediterranean Sea, Denmark Strait, Faroe Bank Channel, Red Sea and the Antarctic (Warren, 1981; Price and Baringer, 1994). Subsequently, many aspects of these overflows have been explored as a result of observational programs (Baringer and Price, 1997; Girton and Käse, 2001; Girton and Sanford, 2003; Gordon et al., 2004; Peters et al., 2005; Peters and Johns, 2005).

The dynamical model for overflows based on the initial observations, namely the Mediterranean Sea and the Denmark Strait overflows, is so-called stream-tube model (Smith, 1975; Killworth, 1977; Price and Baringer, 1994). In this model, the overflow is considered as a homogeneous entity in which the gravitational force is balanced by shear stress at the bottom and entrainment stress at the top, and the Earth's rotation acts to steer the overflow along topographic contours. Since the overflow transport increases between the source and the location of neutral buoyancy, entrainment of ambient fluid is considered as the critical process in the dynamics of all overflows (Price and Baringer, 1994). Much of our present understanding of entrainment in overflows is based on laboratory experiments of bottom gravity currents (Ellison and Turner, 1959; Simpson, 1987; Cenedese et al., 2004; Baines, 2001, 2005). Recent advances in computer power and computational techniques also make possible another approach, so-called large-eddy simulation, in which the turbulent coherent structures that carry out most of the mixing, namely Kelvin–Helmholtz billows and secondary shear instabilities, are explicitly computed (Özgökmen and Chassignet, 2002; Özgökmen et al., 2003, 2004a,b, 2006, 2007). Generally speaking, the bottom drag has been traditionally viewed as a simple frictional mechanism and most of the attention has been paid to the process of entrainment. One of the main contributions of the laboratory and high-resolution numerical experiments is the development of simple representations of entrainment in gravity currents in relation to the gradient Richardson number, $Ri = N^2/S^2$ the ratio of the square of buoyancy frequency and vertical shear, or even simpler, to the bottom slope angle.

The importance of the representation of overflows in OGCMs led to a significant collaborative effort and formation of so-called climate process team on gravity current entrainment (<http://cpt-gce.org/index.htm>). In the context of this collaboration, a number of idealized gravity current experiments (Chang et al., 2005; Ezer, 2005; Legg et al., 2006; Xu et al., 2006) and regional simulations in comparison

to observational overflow data (Xu et al., in press; Chang et al., in press; Riemenschneider and Legg, 2007) are being conducted with the purpose of incorporating parameterizations of overflow entrainment in OGCMs. Two important issues emerged on the basis of these simulations and recent overflow observations that have not been evident thus far. The first is the recognition that overflows are not necessarily homogenous but may have a vertical density structure. In particular, Peters and Johns (2005) partitioned the Red Sea overflow into a so-called bottom layer, in which the densest overflow water is transported, and a so-called interfacial layer, in which turbulent overturning eddies lead to entrainment. The second is the sensitivity of overflow dynamics to the underlying fine-scale details of topography (Ezer, 2006; Riemenschneider and Legg, 2007; Chang et al., in press).

Thus, we pose the following question as the central focus of the present study:

- What is the role of the rough topography in setting the properties of the overflow product water masses, which are of ultimate importance for the large-scale circulation?

To our knowledge, laboratory studies of bottom gravity currents have been conducted only over smooth surfaces. In contrast, the sea-floor morphology exhibits roughness at almost all spatial scales (Weissel et al., 1994). The impact of rough topography on bottom gravity currents was briefly explored by Özgökmen et al. (2004a). However, since these numerical experiments were conducted with a homogenous ambient fluid, neutral buoyancy equilibrium was not attained. Ambient stratification was then incorporated in Özgökmen et al. (2006), albeit with only smooth topography, and the parameters determining the product water mass properties were explored. The results showed that, for the case of constant slope angle and linear ambient stratification, the gravity current separates from the bottom such that the entrained mass flux is independent of the slope angle. The product mass transport and product salinity then depend only on the ambient stratification, and these quantities were approximated as simple algebraic functions of the ambient stratification parameter that modify the source properties.

A surprising finding of the study by Özgökmen et al. (2006) is that the separation level is well estimated by calculating where the densest outflow water would equilibrate in the absence of mixing. This is in contrast with the notion that entrainment dilutes the overflow plume as a whole, and changes the geo-potential level at which the plume joins the general circulation. Here, we put forth that the result of Özgökmen et al. (2006) is because the turbulent overturning eddies, resulting from the shear instability, are typically smaller than the thickness of the gravity current, and are unable to reach all the way to the bottom of the plume (Fig. 1). To quantify this statement, we remember that Gargett et al. (1984) have shown that the largest

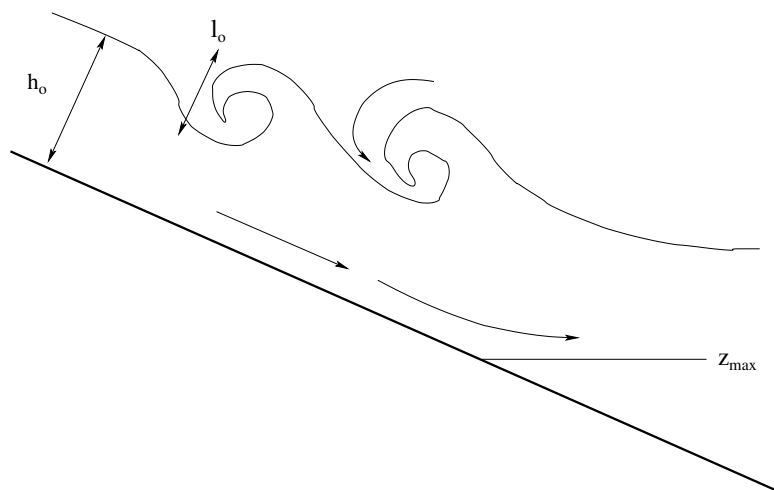


Fig. 1. Schematic illustration of the idea that in the case that stratified overturning scale l_0 is smaller than the gravity current thickness h_0 , the densest bottom waters escape dilution and set the separation depth z_{max} .

overturning scale in stratified mixing is set by the Ozmidov scale $\ell_O = \sqrt{\varepsilon/N^3}$, where ε is the turbulent kinetic energy dissipation rate and N is the buoyancy frequency. By dimensional arguments, ε can be estimated from $\varepsilon = c_\varepsilon u_0^3/\ell$, where u_0 is a characteristic velocity of energy-containing turbulent eddies, ℓ is their characteristic length scale, and c_ε is a proportionality constant (Taylor, 1935; Pope, 2000). While this scaling was originally introduced for homogeneous fluids, it is expected to hold for stratified fluids as well (Gargett, 1994) by setting $\ell \approx \ell_O$. The upper bound for the characteristic eddy velocity u_0 is assumed to be given by the initial propagation speed of the gravity currents $u_0 = \sqrt{\frac{g\Delta\rho'h_0}{2\rho_0}}$ (Benjamin, 1968; Özgökmen et al., 2004b). In order to obtain an upper bound for the overturning scale, the buoyancy frequency N can be expressed as $N = \sqrt{-\frac{g}{\rho_0} \frac{\partial\rho'}{\partial z}} \approx \sqrt{\frac{g}{\rho_0} \frac{\Delta\rho'}{\ell_O}}$. Regarding the estimates for c_ε , the range of $0.67 \leq c_\varepsilon \leq 0.79$ is most common (Moum, 1996). Using this range, we obtain a maximum scale for the overturning eddies as

$$\frac{\ell_O}{h_0} \approx 0.5c_\varepsilon^{2/3} \quad \text{or} \quad 0.38 \leq \frac{\ell_O}{h_0} \leq 0.43. \quad (1)$$

Thus, we conclude that shear instability taking place at the top is probably not the most efficient or direct mechanism to influence the properties at the bottom of the overflow plume. Subsequently, the water masses near the bottom, which are also the densest, escape dilution and set the separation level (Fig. 1).

In this study, we explore the effect of bottom roughness on the neutral buoyancy equilibrium level of overflow product waters in a non-rotating environment. We approach this problem using the three-dimensional (3D) non-hydrostatic spectral element model Nek5000 developed by Fischer (1997b). Since this investigation is a natural continuation of two previous studies (Özgökmen et al., 2004a, 2006), the model configurations are quite similar. The experiments are carried out in a parameter matrix consisting of the amplitude of bottom roughness and the strength of ambient stratification. The main finding of this investigation is that bottom roughness can facilitate the dilution of the densest water masses, and significantly influence the separation level from the bottom. Another, and somewhat unexpected finding, is that the form drag resulting from flow separation around rough bottom topography can be as important as the bottom shear drag for the dynamics of the overflows. To our knowledge, form drag has never been quantified from observations of oceanic overflows since very high spatial resolution pressure measurements are needed.

The paper is organized as follows. The numerical model introduced in Section 2. The experimental setup and parameters are outlined in Section 3. Results are presented in Section 4, and the principal results and future directions are summarized in Section 5.

2. Numerical model

Nek5000 combines the high-order accuracy of spectral methods with the geometric flexibility of traditional finite element methods. The code integrates unsteady incompressible Navier–Stokes equations within the Boussinesq approximation. Moreover, Nek5000 handles general three-dimensional flow configurations, supports a broad range of boundary conditions for hydrodynamics, and accommodates multiple-species (passive or active tracer) transport. Here, we give a short description of this code.

The momentum and continuity equations subject to the Boussinesq approximation can be written as follows:

$$\frac{D\mathbf{u}}{Dt} = -\frac{1}{\rho_0} \nabla p + \nu_h \nabla_r^2 \mathbf{u} - g \frac{\rho'}{\rho_0} \hat{\mathbf{z}}, \quad (2)$$

$$\nabla \cdot \mathbf{u} = 0 \quad (3)$$

where $\mathbf{u} = (u, v, w)$ is the velocity vector field; p the pressure; $g = 9.81 \text{ m s}^{-2}$, the gravitational acceleration; ν_h the viscosity in the horizontal direction; and $\hat{\mathbf{z}}$ the unit normal vector in vertical direction. The material (total) derivative is

$$\frac{D}{Dt} := \frac{\partial}{\partial t} + \mathbf{u} \cdot \nabla, \quad (4)$$

and the anisotropic diffusivity is

$$\nabla_r^2 := \frac{\partial^2}{\partial x^2} + \frac{\partial^2}{\partial y^2} + r \frac{\partial^2}{\partial z^2}, \quad (5)$$

where $r := \nu_v/\nu_h$ is the ratio of vertical to horizontal eddy viscosities. The numerical simulations in this study are in the category of large-eddy simulation, in which the turbulent coherent structures that carry out most of the stirring are explicitly computed and the impact of smaller-scale, unresolved features on the resolved flow field is represented using subgrid-scale (SGS) models. The anisotropic Laplacian is a simple SGS model to represent the peculiar dynamics of stratified flows, in particular the anisotropic mixing, used also in Özgökmen and Chassignet (2002), Özgökmen et al. (2003, 2004a,b, 2006). Recently, a more comprehensive investigation of the effect of different SGS models on mixing in stratified flows is carried out by Özgökmen et al. (2007). It is found by a systematic comparison to direct numerical simulations that the performance of SGS models can differ somewhat, and in particular, SGS models can lead to an improvement with respect to the case when no SGS models are used (so-called under-resolved direct numerical simulation). Nevertheless, it is also shown that a significant decline in capturing the long-term probability distribution of density perturbation arising from mixing occurs only when Kelvin–Helmholtz billows are not resolved. This happens when the mesh spacing exceeds the Ozmidov scale. High-resolution simulations conducted here ensure that overturning eddies are resolved, and the simple SGS model (5) is deemed adequate for the purposes of this study.

A linear equation of state

$$\rho' = \rho_0(\beta S - \alpha T) \quad (6)$$

is used, where ρ_0 is the background water density; $\beta = 7 \times 10^{-4} \text{ psu}^{-1}$ and $\alpha = 2 \times 10^{-4} \text{ }^\circ\text{C}^{-1}$ are the salinity contraction and temperature expansion coefficients, respectively; and S and T are salinity and temperature deviations from a background value, respectively. The equations for salinity and heat transport are

$$\frac{DS}{Dt} = K_h \nabla_r^2 S, \quad (7)$$

and

$$\frac{DT}{Dt} = K_h \nabla_r^2 T, \quad (8)$$

where we assume that the vertical and horizontal eddy diffusivities also satisfy $r = K_v/K_h$, and K_h and K_v are the same for temperature and salinity.

The time advancement of (2)–(8) is based on second-order semi-implicit operator-splitting methods developed by Maday et al. (1990) and described by Fischer (1997a). The hydrodynamics (2)–(4) are advanced first, with explicit treatment of the buoyancy forcing term, followed by the update of the salinity and temperature transport. Spatial discretization is based on the spectral element method (Patera, 1984; Maday and Patera, 1989; Fischer, 1997b), which is a high-order weighted residual technique based on compatible velocity and pressure spaces free of spurious modes. Locally, the spectral element mesh is structured, with the solution, data, and geometry expressed as sums of N th-order Lagrange polynomials on tensor-products of Gauss or Gauss–Lobatto (GL) quadrature points. Globally, the mesh is an unstructured array of K deformed hexahedral elements and can include geometrically non-conforming elements. For problems having smooth solutions, the spectral element method achieves exponential convergence with N , despite having only C^0 continuity (which is advantageous for parallelism). The convection operator exhibits minimal numerical dissipation and dispersion, which is important for high-Reynolds number applications.

The spectral element method offers a dual approach to convergence: algebraic via elemental grid refinement, and exponential via increase in the order of intra-element interpolation. The number of elements are chosen to capture the shape of the domain geometry is adequately and the element size is also adjusted to better capture the bottom boundary layer. Then, the spectral truncation degree is increased for numerical accuracy. In general, the numerical solution of the physical problem of interest benefits from two well-known features of spectral element models: the lack of numerical dissipation and excellent phase properties. In the present study, the geometric flexibility of the model is also of critical importance.

Efficient solution of the Navier–Stokes equations in complex domains depends on the availability of fast solvers for sparse linear systems. Nek5000 uses as a preconditioner the additive overlapping Schwarz method

introduced by Dryja and Widlund (1987) and developed in the spectral element context by Fischer and Ronquist (1994), Fischer (1997b), Fischer and Gottlieb (1997) and Lottes and Fischer (2005). The key components of the overlapping Schwarz implementation are fast local solvers that exploit the tensor-product form and a parallel coarse-grid solver that scales to thousands of processors (Tufo and Fischer, 2001). The capabilities of the spectral element method have been significantly enhanced through the recent development of a high-order filter that stabilizes the method for convection dominated flows without compromising spectral accuracy (Fischer and Mullen, 2001). More details on the solution procedure of Nek5000 in the context of gravity current simulations can be found in Özgökmen et al. (2004b).

3. Model configuration and parameters

Our primary purpose is to determine the effect of rough topography on the overflow product water masses. To achieve this objective, numerical experiments are conducted in a matrix consisting of the ambient stratification gradient and the amplitude of the topographic perturbations superimposed on the sloping portion of the domain. The overflow is represented using a salinity anomaly whereas the interior fluid is initially stratified using a linear temperature gradient. Such a decomposition of the density structure allows for a convenient identification of the overflow, in particular after neutral equilibrium is reached. Unlike in Özgökmen et al. (2006), in which predominantly 2D experiments were conducted for computational efficiency, all experiments are 3D here in order to fully represent the effects of turbulent flows.

The domain geometry, boundary conditions, initialization and most of the parameters are based on those used in Özgökmen et al. (2004a, 2006, 2004b). For the purpose of brevity, we refer the reader to these papers for all details and justification, and only outline the differences here. The model domain is configured with a horizontal length of $L_x = 15$ km and span-wise width of $L_y = 2$ km. The depth of the water column ranges from $h_i = 400$ m at $x = 0$ to $H = 1000$ m over a constant slope (Fig. 2). A salinity anomaly with an amplitude of $\Delta S = 1$ psu and initial thickness of $h_0 = 200$ m is placed at the top of the slope. A sinusoidal perturbation in the initial salinity distribution in the y -direction is employed to facilitate transition to 3D turbulent flow. The saline inflow is sustained by a dynamic boundary condition, which is the main forcing driving the system. For experiments over smooth topography, a background slope angle of $\theta = 3^\circ$ (or slope $\tan \theta = 0.0524$) is used (Fig. 2a), which is within the general range of oceanic overflows prior to their separation from the bottom, such as the Red Sea overflow entering the Tadjura Rift (Özgökmen et al., 2003). Geometries with smaller slope angles require a longer domain, and are computationally more expensive. For experiments with rough topography, sinusoidal perturbations are superimposed on the background topography between $x_1 = 1.45$ km and $x_2 = 11.45$ km of the form

$$\frac{\eta(x,y)}{H} = a \sin(2\pi k_x(x - x_1)) \cos(2\pi k_y y) \quad \text{for } x_1 \leq x \leq x_2 \text{ and } 0 \leq y \leq L_y, \quad (9)$$

with wavenumbers $k_x = 1 \text{ km}^{-1}$, $k_y = 1 \text{ km}^{-1}$ and non-dimensionalized (by H) amplitude $a = 0.1; 0.2; 0.4; 0.6$ (Fig. 2b–e; perturbations exceeding the domain range are clipped off). The main reason for choosing this topography is simplicity. It is not possible to put forth a single generic representative function given the complexity of the Earth's topography (Weissel et al., 1994). While the quantitative results are likely to depend on the details of topographic perturbations, the concept of whether and how rough topography affects the overflow should be essentially independent of the choice of (9).

Model parameters are most efficiently described in terms of non-dimensional numbers $Ra = (g\beta\Delta S h_0^3)/\nu_h^2$ the Rayleigh number, the ratio of the strengths of buoyancy and viscous forces, $Pr = \nu_h/K_h$ the Prandtl number, the ratio of viscosity and diffusivity, $r = \nu_v/\nu_h = K_v/K_h$ the diffusivity ratio, and $R_\rho = (\alpha\Delta T h_0)/(\beta\Delta S H)$ the density ratio, the ratio of the density gradients due to ambient temperature stratification and overflow salinity stratification. These parameters are mostly identical to those in Özgökmen et al. (2006) and are listed in Table 1.

The ambient fluid is initially stratified by using a linear temperature profile of the form $T = \Delta T(\frac{z}{H} + 1)$ with $-H \leq z \leq 0$. Four values of density ratios are used, $R_\rho = 0.34; 0.4; 0.6; 0.8$, which correspond to temperature differences between the top and bottom of the domain of $\Delta T = 5.95^\circ\text{C}; 7^\circ\text{C}; 10.5^\circ\text{C}; 14^\circ\text{C}$, respectively. The

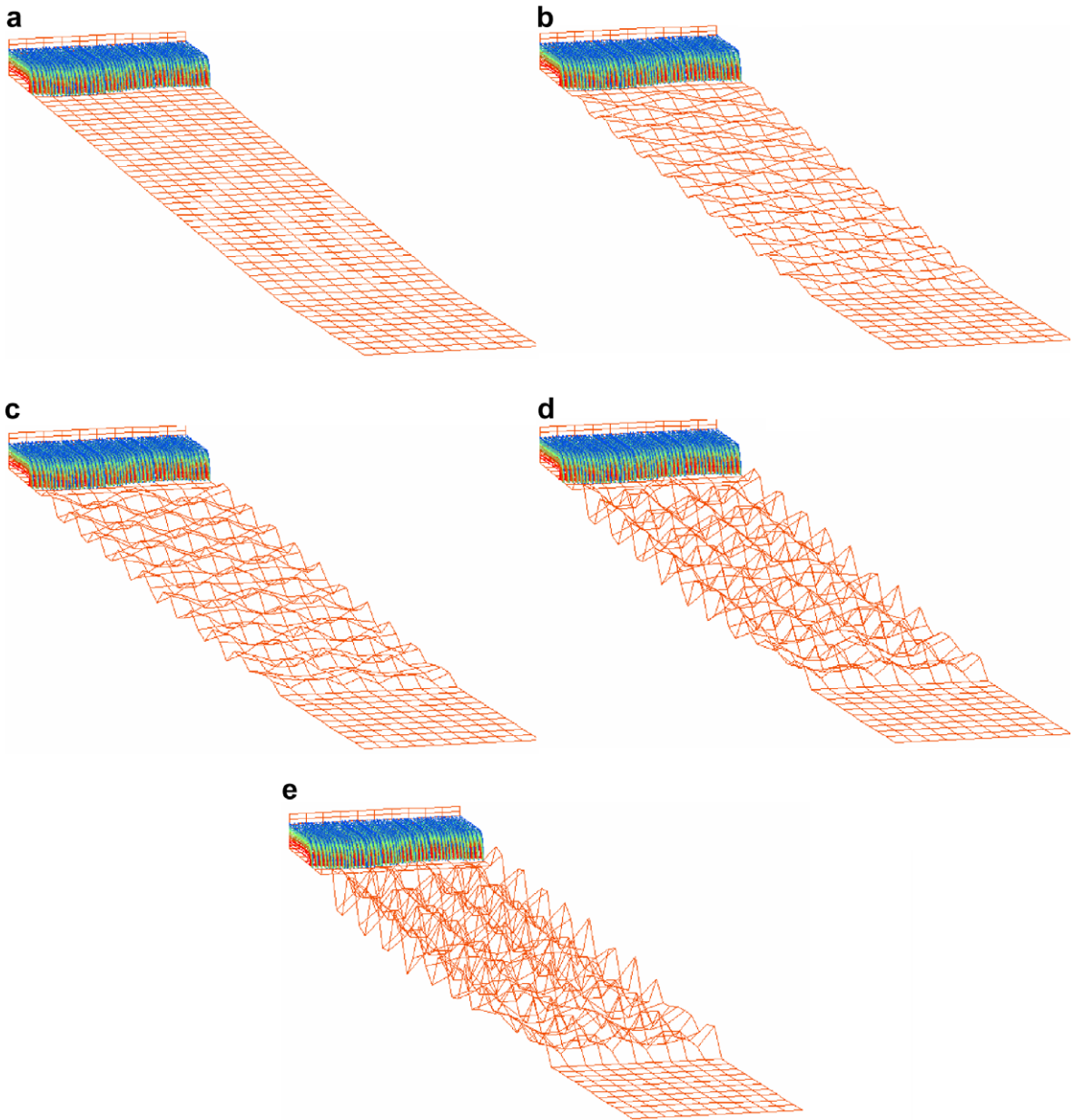


Fig. 2. Model domain for: (a) $a = 0$, (b) $a = 0.1$, (c) $a = 0.2$, (d) $a = 0.4$, (e) $a = 0.6$.

separation depth of the overflow can be estimated a priori by calculating where the densest overflow water mass would equilibrate in the ambient fluid in the absence of mixing, and this can be written as (Özgökmen et al., 2006):

$$z_{\max} = -h_i - \frac{h_0}{R_\rho} \quad \text{and} \quad x_{\max} = \frac{H}{R_\rho \tan \theta}. \quad (10)$$

For the selected stratifications of $R_\rho = 0.34; 0.4; 0.6; 0.8$, the separation from the bottom is expected to take place at levels of $z_{\max} = -988 \text{ m}, -900 \text{ m}, -733 \text{ m}$ and -650 m , respectively. This covers the full range

Table 1

Parameters of the numerical simulations

Domain size ($L_x, L_z = H, L_y$)	15×10^3 m, 10^3 m, 2×10^3 m
Background slope angle	$\theta = 3^\circ$
Rayleigh number	$Ra = 8 \times 10^5$
Prandtl number	$Pr = 1$
Diffusivity ratio	$r = 5 \times 10^{-2}$
Density ratios	$R_\rho = 0.34, 0.40, 0.60, 0.80$
Viscosities	$\nu_h = 0.83 \text{ m}^2 \text{ s}^{-1}$ and $\nu_v = 1.66 \times 10^{-2} \text{ m}^2 \text{ s}^{-1}$
Diffusivities	$K_h = 0.83 \text{ m}^2 \text{ s}^{-1}$ and $K_v = 1.66 \times 10^{-2} \text{ m}^2 \text{ s}^{-1}$
Overflow salinity range	$\Delta S = 1.0$ psu
Overflow input thickness	$h_0 = 200$ m
Overflow source depth	$h_i = 400$ m
Ambient temperature range	$\Delta T = 5.95, 7, 10.5, 14$ °C
Ambient buoyancy period	$T_b = 1838(31), 1694(28), 1383(23), 1198(20)$ s (min)
Number of elements (x, z, y)	52, 8, 10
Polynomial degree	$N = 6$
Number of grid points	898,560
Bottom roughness amplitude	$a = 0, 0.1, 0.2, 0.4, 0.6$
Time step	$\Delta t = 1.2$ s
Total integration time	20,000–30,000 s

of available depths, considering that $H = 1000$ m, $h_i = 400$ m and $h_0 = 200$ m. The model is integrated for a total period τ until the separated gravity currents reach the end of the domain, which typically takes between 20,000 s and 30,000 s, depending on the propagation speed. With respect to the ambient buoyancy period $\tau_b = 2\pi/N$, where $N = \sqrt{g\alpha\Delta T/H}$, the integration period is about an order of magnitude longer, $11 \leq \frac{\tau}{\tau_b} \leq 25$ (Table 1).

The rotation time scale would be $2\pi f_0^{-1} \approx 29 \times 10^4$ s and 6×10^4 s at selected low (10°N) and high (60°N) latitudes, respectively. The period for the flow to fully develop is too short for rotational effects to become important, and the corresponding deformation radii are too large to fit in the computational domain. This is fundamentally a scale separation issue in that not all space and time scales can be captured simultaneously due to computational limits, and compromises are inevitable. Here, we opt for the resolution of turbulent overturning eddies at the expense of the larger scale dynamics, in recognition that it is the diapycnal mixing that determines the water mass properties while rotation influences mainly the large-scale pathways. Thus, the effect of rotation is neglected in this study.

The discretization is via $K = 4160$ elements ($52 \times 8 \times 10$ in x, z, y directions) and a spectral truncation with a polynomial degree of $N = 6$. This corresponds to a total of 898,560 grid points. The elements have a smaller vertical scale toward the bottom boundary and follow topography. With a time step of $\Delta t = 1.2$ s, the Courant number remains conservatively $C < 1$ throughout the simulations (the model can sustain $C \approx 2$ due to semi-implicit operator-splitting time advancement). The computational time is proportional to KN^4 . Each experiment took about 4 days in real time (equivalent to a computed versus real time ratio of approximately 0.1) on 16 processors of our local cluster. Output from one every hundred time steps is recorded, which corresponds to a storage requirement of about 12GB per experiment. Because of this computational expense, the following results are based on a total of 12 experiments (Table 2).

Table 2

List of experiments

	$a = 0$	$a = 0.1$	$a = 0.2$	$a = 0.4$	$a = 0.6$
$R_\rho = 0.34$	✓	–	✓	–	✓
$R_\rho = 0.40$	✓	✓	✓	✓	✓
$R_\rho = 0.60$	✓	–	✓	–	–
$R_\rho = 0.80$	✓	–	✓	–	–

4. Results

4.1. Description

Distributions of salinity anomaly in experiments with smooth and rough bottom topography are shown in Figs. 3 and 4 for the case with $R_\rho = 0.4$. The behavior of density currents over smooth topography is better understood than those over rough topography. The system starts as in so-called dam-break (or lock-exchange) problem (Keulegan, 1958; Simpson, 1987; Özgökmen et al., 2007) and rapidly forms a characteristic head at the leading edge (e.g., Fig. 3a) and shear instabilities in the trailing fluid. Both types of coherent features lead

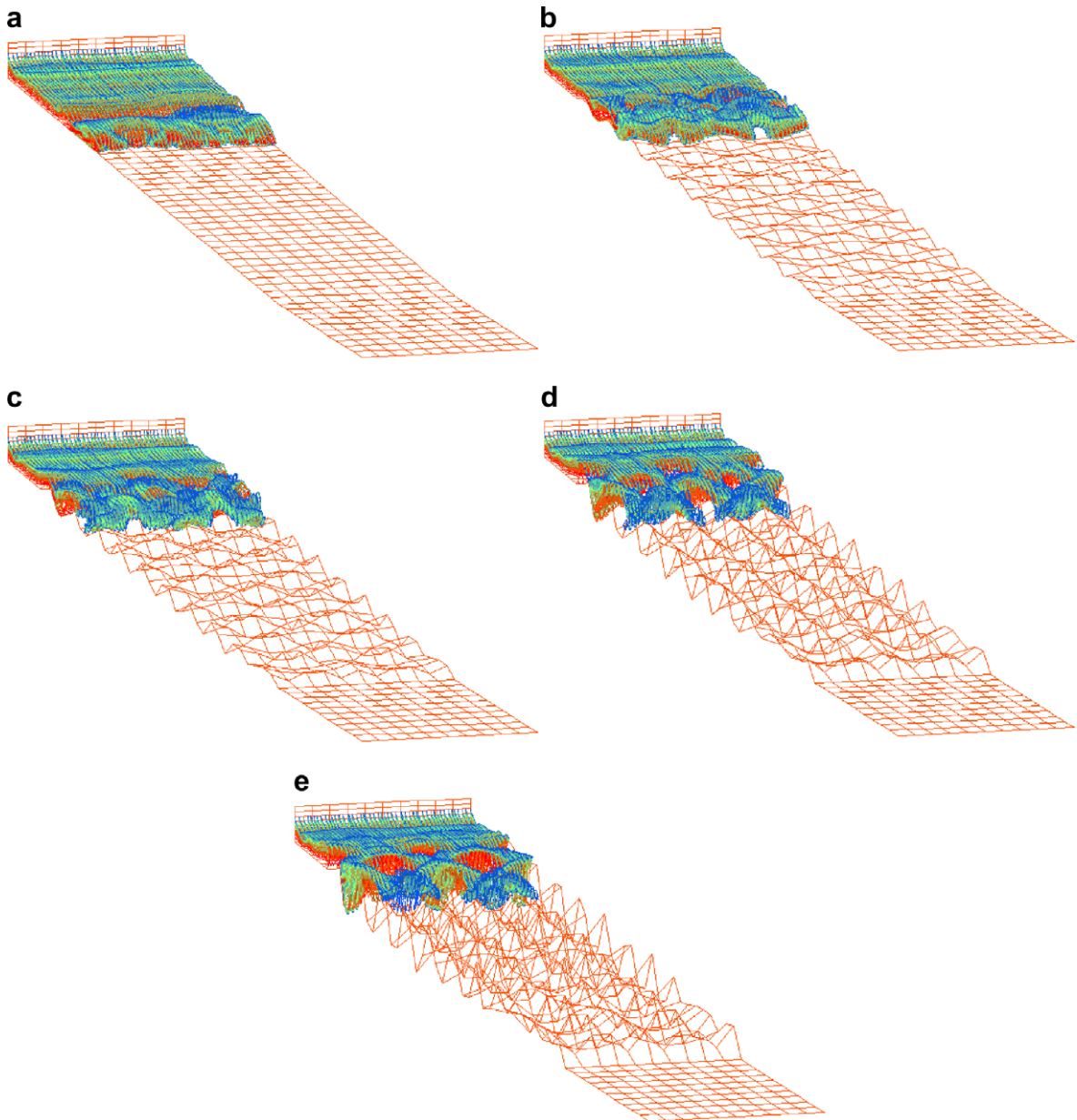


Fig. 3. Distribution of the salinity anomaly at $t = 3720$ s in cases with: (a) $a = 0$, (b) $a = 0.1$, (c) $a = 0.2$, (d) $a = 0.4$, (e) $a = 0.6$, and $R_\rho = 0.4$. Animations are available from <http://www.rsmas.miami.edu/personal/tamay/3D/tsb.html>.

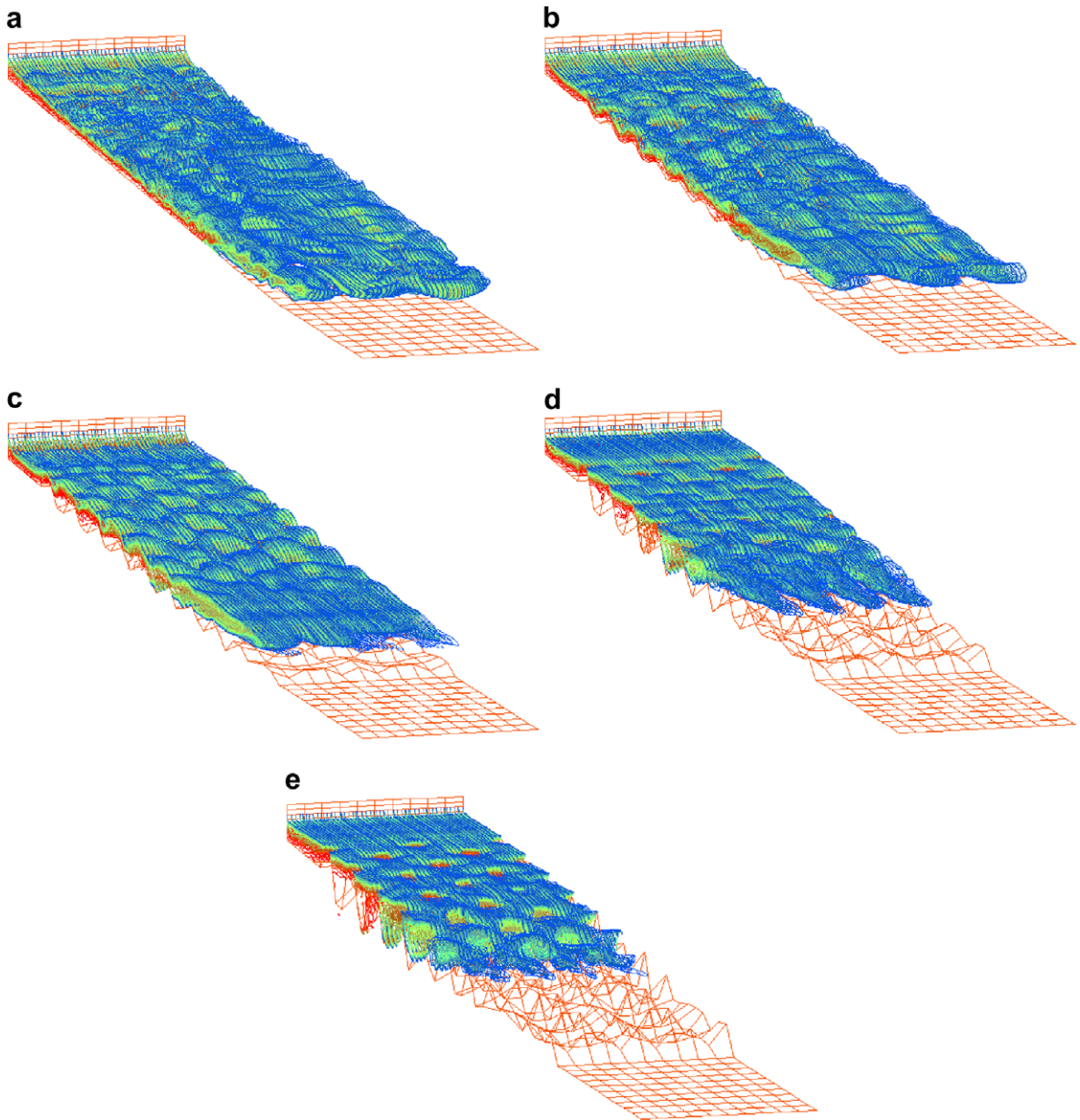


Fig. 4. Distribution of the salinity anomaly at $t = 18,000$ s in cases with: (a) $a = 0$, (b) $a = 0.1$, (c) $a = 0.2$, (d) $a = 0.4$, (e) $a = 0.6$, and $R_p = 0.4$.

to entrainment of ambient fluid into the gravity current (see Fig. 11 of (Özgökmen and Chassignet (2002))). The initial shear instability is basically of the form of 2D Kelvin–Helmholtz rollers. If constrained to 2D, Kelvin–Helmholtz rolls tend to grow by pairing (Klaassen and Peltier, 1989), while in 3D, secondary modes of instability arise. In particular, the stream-wise vortices stretch and tilt the span-wise vorticity, which is concentrated in Kelvin–Helmholtz rolls. Consequently, Kelvin–Helmholtz rolls cannot sustain their lateral coherence and break down (Klaassen and Peltier, 1991; Fritts et al., 1998; Andreassen et al., 1998), resulting in the evolution of increasingly more complex turbulent coherent structures, which are visible at the outer interface of the salinity anomaly defining the gravity current (Fig. 4a). Before the gravity current reaches the end of the domain, the nose of the current lifts off the bottom and starts propagating at the level of neutral buoyancy.

The change in direction also results in the reduction of gravitational force acting on the current, and the forward propagation speed reduces. The propagation is maintained for reasons of mass conservation, or due to the pressure exerted by the thickness of the incoming gravity current accumulating near the separation point.

Several important differences can be observed in cases of rough topography (Fig. 4b–e). First, the propagation speed appears to have been reduced, which is particularly clear from Fig. 4e in comparison to Fig. 4a. Second, the separation from the bottom seems to take place over a shorter distance along the slope (or higher up in the water column). Third, the turbulent overturning structures at the interface between the overflow and ambient fluid seem to become less pronounced, and instead, the spatial scales of the underlying topographic roughness appear to govern the salinity field. Similar changes occur for all cases of R_ρ (e.g., see Fig. 5 for $R_\rho = 0.6$), with the separation level moving upward in the water column and turbulent overturning scales decreasing in size when the ambient stratification gradient R_ρ is increased, as discussed in Özgökmen et al. (2006).

The first observation implies that there is added drag on the flow field in the case of rough topography. The second point indicates that the product salinity is modified with respect to the case of smooth topography. The third puts forth a question on the nature of mixing. These issues are investigated and quantified below.

4.2. Propagation speed

The propagation of bottom gravity currents over smooth topography is well understood. In the case of homogeneous ambient fluid, gravity currents achieve a nearly constant speed of descent under the force gravity balanced by shear stress at the bottom boundary, and entrainment stress at the interface with the overlying fluid. As shown by Britter and Linden (1980), the propagation speed is fairly insensitive to the slope angle, as the change in the direction of gravitational force acting on fluid parcels is compensated by the change in their buoyancy via entrainment, which is approximately linearly proportional to the slope angle. In the case of down-slope motion in a stratified environment, the propagation speed decreases with increasing fluid depth, as denser ambient fluid is encountered (Özgökmen et al., 2006).

The position of the salinity front as a function of time, $X_F(t)$, is plotted in Fig. 6a for all cases with $R_\rho = 0.4$, namely those with $a = 0; 0.1; 0.2; 0.4; 0.6$. The gravity current flow over smooth topography shows three distinct regimes of propagation. The first regime ($1 \text{ km} \leq X_F \leq 5 \text{ km}$) is one of nearly-constant (if not accelerating) propagation, followed by a slow reduction in speed ($5 \text{ km} < X_F \leq 12 \text{ km}$) due to increase in fluid density with depth, and finally a significant rate of reduction in the propagation speed, which coincides with the separation of the plume from the bottom. The main result depicted in Fig. 6a is that topographic roughness can cause a significant reduction in propagation speed of the gravity current. Results from experiments with different R_ρ are conceptually similar (Fig. 6b). The initial propagation speed is nearly identical in all cases. For cases with smooth topography, changes occur due to differences in the strength of the ambient stratification. In all cases, rough topography causes further reduction in propagation speed.

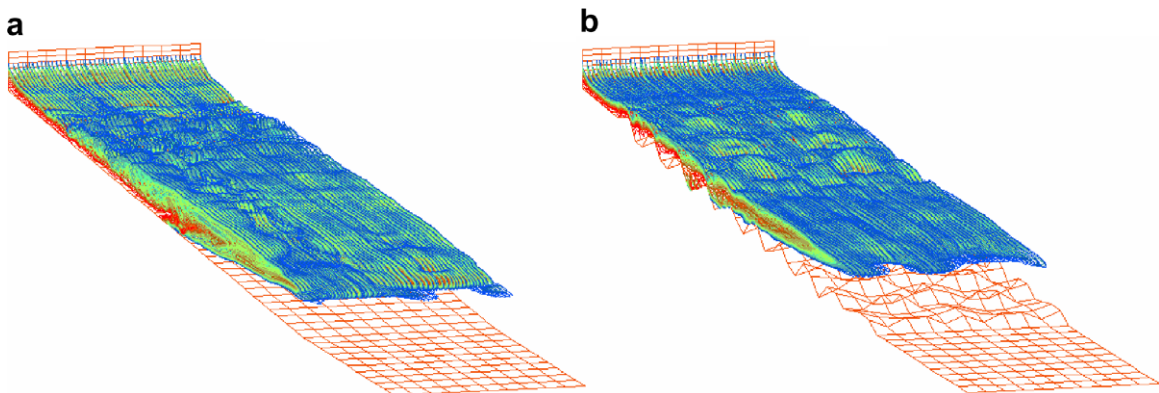


Fig. 5. Distribution of the salinity anomaly at $t = 18,000 \text{ s}$ in cases with: (a) $a = 0$, (b) $a = 0.2$ and $R_\rho = 0.6$.

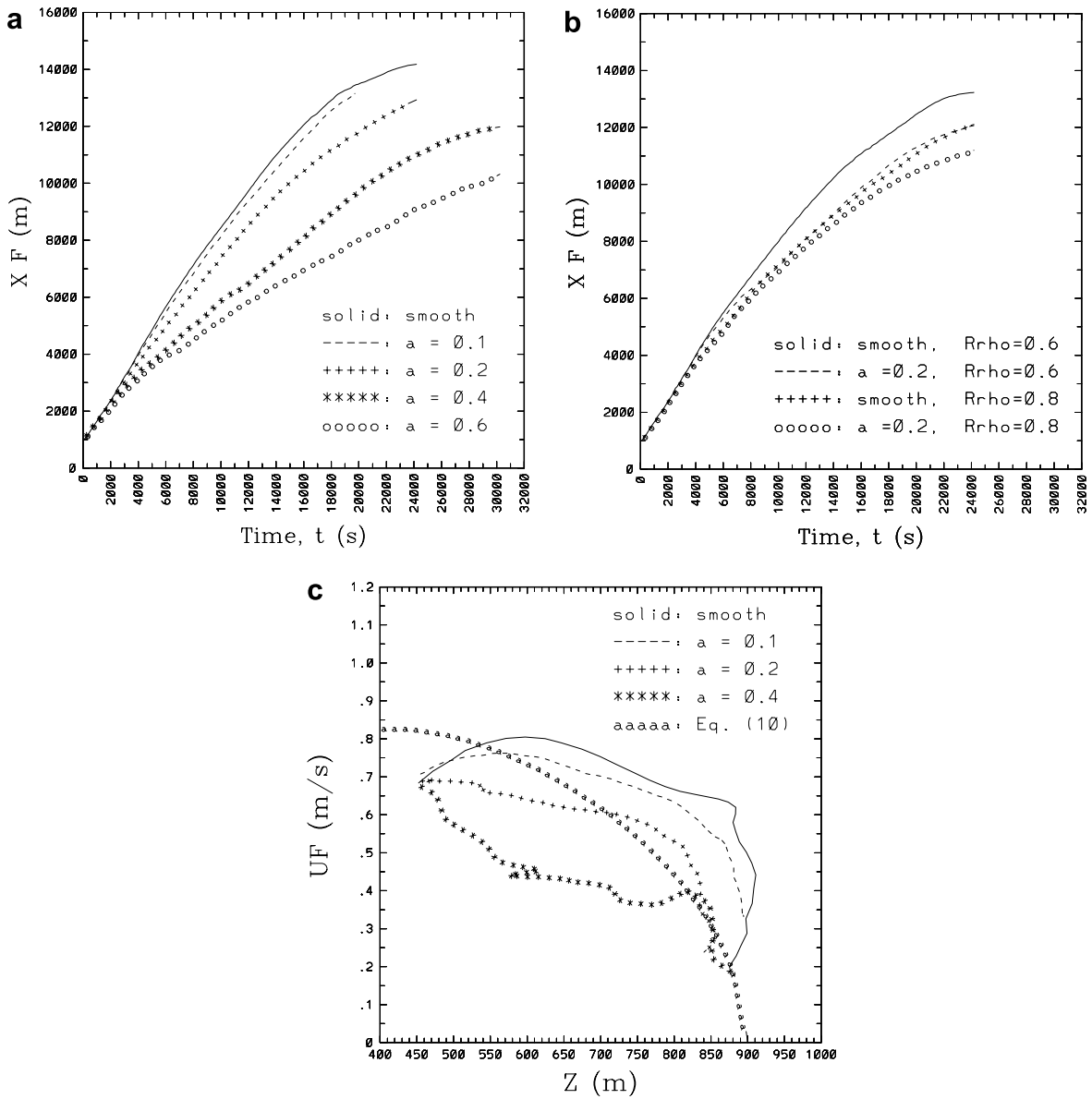


Fig. 6. Position of the salinity front $X_F(m)$ as a function of time for experiments with: (a) $R_\rho = 0.4$, and (b) $R_\rho = 0.6$ and $R_\rho = 0.8$. (c) Propagation speed of the salinity front U_F (m s⁻¹) as a function of mean fluid depth z in experiments with $R_\rho = 0.4$, and as estimated from (11).

The propagation speed, $U_F(t) = dX_F/dt$, in a two-layer system is approximately given by $U_F = \sqrt{g'h_0(z' - h_0)/z'}$ (Benjamin, 1968), where z' is the total fluid depth at the salinity front. Here, z' is in the range of $h_i \leq z' \leq \frac{h_0}{R_\rho}$ between the inlet and expected separation points. We note that $h_i \approx 2h_0$ in these experiments. The reduced gravity is $g' = g(\rho'_o - \rho'_a)$, where the initial density perturbation associated with the overflow is $\rho'_o = \beta\Delta S - \alpha\Delta T(1 - h_i/H)$ and ambient density perturbation is $\rho'_a = -\alpha\Delta T(1 - z'/H)$. Thus, we obtain

$$\frac{U_F}{\sqrt{g\beta\Delta Sh_0}} = \sqrt{1 - R_\rho \left(\frac{z' - h_i}{h_0}\right) \left(1 - \frac{h_0}{z'}\right)} \quad \text{for } h_i \leq z' \leq h_i + \frac{h_0}{R_\rho}, \quad (11)$$

where the last factor on the right-hand-side quantifies the effect of the increase in fluid depth along the path, which can cause an acceleration during the initial phase.

$U_F(z')$ is quantified in experiments with $R_\rho = 0.4$ in Fig. 6c. The expression (11) provides a reference pattern for the case with $a = 0$, with differences being primarily due to initialization, namely a stratified (rather than homogenous) density current between $0 \leq x \leq 1$ km (see Fig. 1b in Özgökmen et al. (2006)). Fig. 6c illustrates that topographic roughness can reduce the speed of propagation to nearly half of that over smooth topography. It is shown below that this difference arises due an added drag force.

4.3. Separation level

The level at which the gravity current lifts off the bottom is determined not only by where the overflow density equals the ambient flow density, but also by the momentum of overflow water parcels while encountering those from the ambient. The overflow momentum is a function of the inflow forcing. If no fluid is supplied through the inflow boundary, then the problem is one of the flow of the initial saline water mass placed at the top of the slope (Fig. 2). In this case, the overflow becomes gradually thinner and slower, due to reasons of mass conservation, with respect to the case, in which fluid is supplied through the inflow boundary to replenish the propagating salinity front. In the latter case, gravity currents can exceed the neutral buoyancy level and exhibit so-called overshoot and spring-back phenomenon (Bloomfield and Kerr, 1998; Baines, 2002). Also the entrainment characteristics are known to differ between so-called constant-volume and constant-flux plumes (Hallworth et al., 1996). Here, the effect of topographic roughness is isolated in comparison to reference experiments over smooth topography under otherwise identical conditions.

The span-wise averaged coordinates $z_{\max}(t)$ and $x_{\max}(t)$ of the salinity fronts in contact with the bottom are plotted in Fig. 7 for experiments with $R_\rho = 0.4$. In the case of smooth topography, the overflow plume reaches a maximum depth that is approximately given by (10). There appears to be a spring-back phenomenon towards the end of the experiment, which could be also caused because the nose of the separated plume is in close proximity to the outflow boundary (Fig. 4a). Computations are terminated when the plumes reach the outflow boundary, because development of appropriate outflow boundary conditions for entraining gravity currents demands assumptions about conditions outside of the computational domain, and this information is likely to influence the simulation. This is not only an ill-posed problem, but also not critical for the purposes of the present study.

It can be clearly seen from Fig. 7a that topographic perturbations change the separation level such that the plumes appear to reach equilibrium higher up in the water column as the roughness amplitude a is increased.

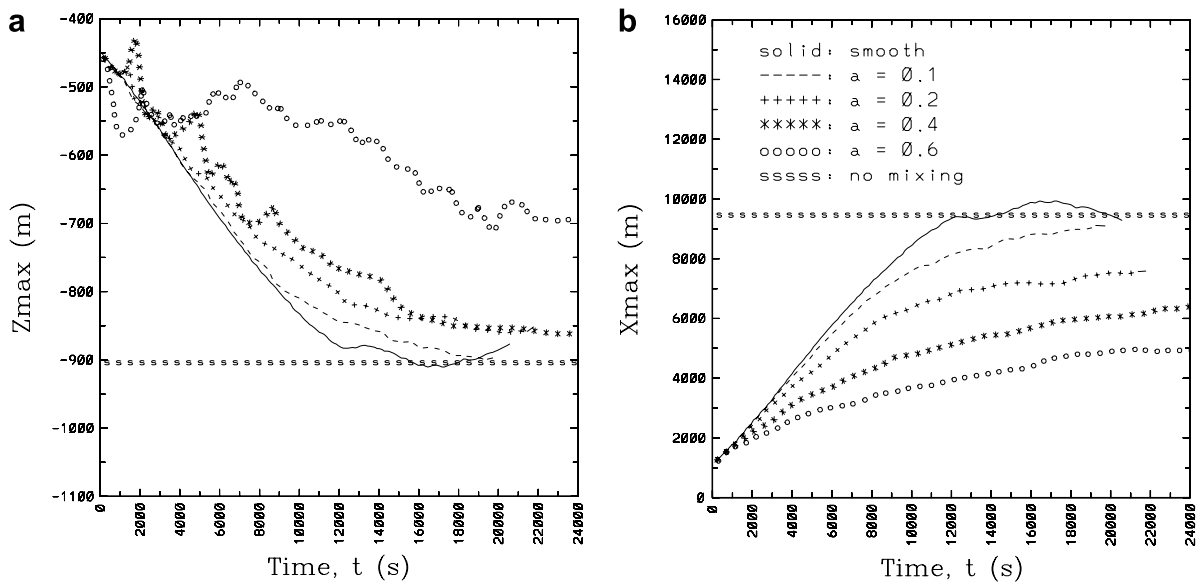


Fig. 7. Maximum distances (a) z_{\max} and (b) x_{\max} of the salinity front over the slope as a function of time in experiments with $R_\rho = 0.4$. Lines with “sss” denote those obtained from (10).

However, there are issues with looking only at z_{\max} in the presence of large-amplitude topographic roughness. Therefore, it is also useful to plot the maximum distance reached by the plumes along the slope. Fig. 7b supplements the results from Fig. 7a in that topographic roughness can cause a significant change in the location, where the gravity currents separate from the bottom topography. Namely, the larger is the topographic roughness, the shorter is the distance down the slope (or down in the water column) the overflows propagate before lifting off. Results from simulations with other R_ρ are also consistent with this trend (Fig. 8). The approximate times when the separation commences are listed in Table 3.

4.4. Product salinity distribution

The results presented in the previous section imply that the overflow properties must have been significantly modified in cases of rough topography such that neutral buoyancy equilibration takes place at different

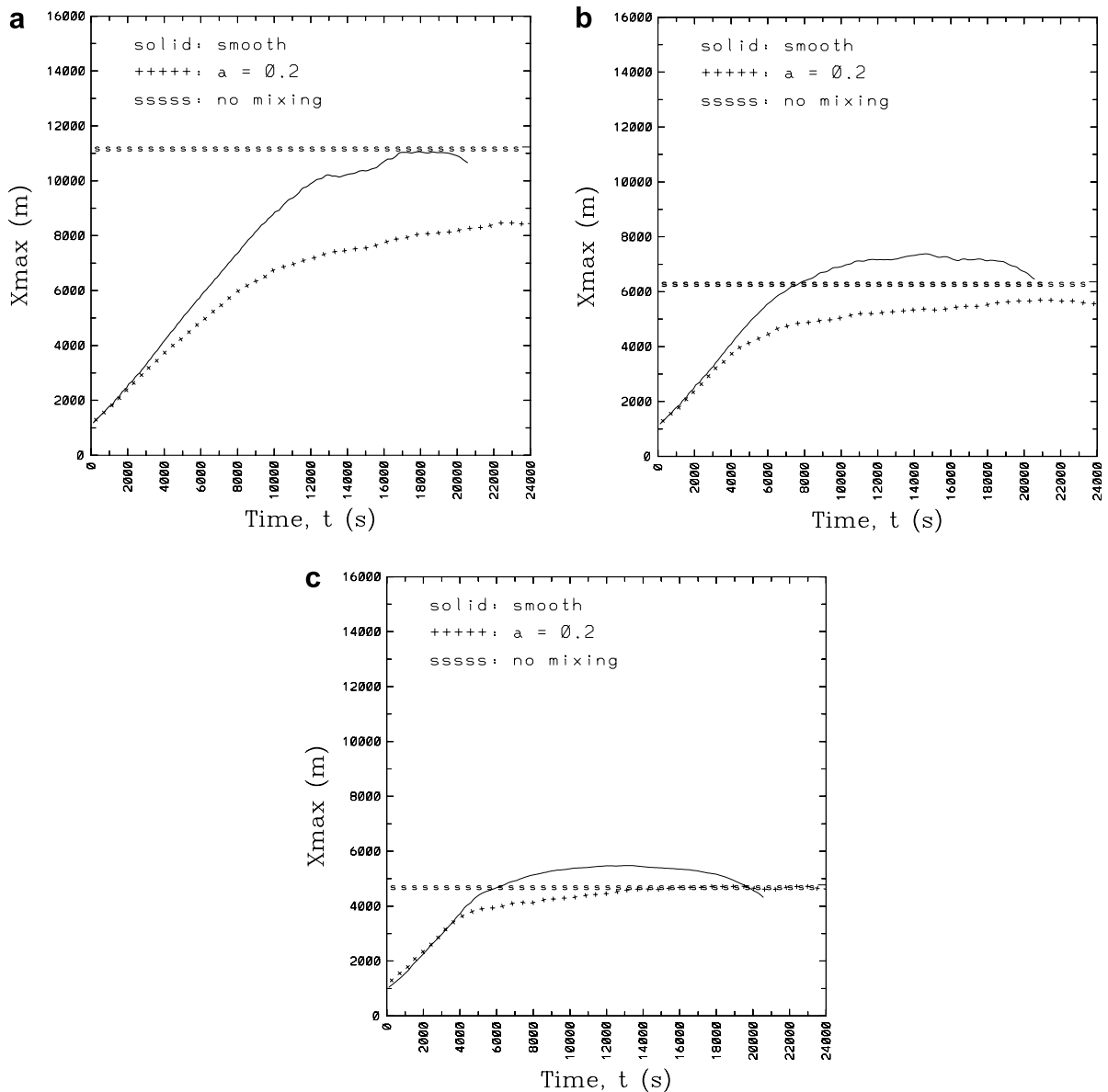


Fig. 8. Maximum distances $x_{\max}(t)$ of the salinity front over the slope in experiments with: (a) $R_\rho = 0.34$, (b) $R_\rho = 0.6$, and (c) $R_\rho = 0.8$.

Table 3
Approximate times when separation commences in all numerical experiments

	$a = 0$ (s)	$a = 0.1$ (s)	$a = 0.2$ (s)	$a = 0.4$ (s)	$a = 0.6$ (s)
$R_p = 0.34$	11,000	–	11,000	–	11,000
$R_p = 0.40$	9000	8500	8000	11,000	14,000
$R_p = 0.60$	7000	–	6500	–	–
$R_p = 0.80$	6600	–	6000	–	–

locations compared to the case over smooth topography. Therefore it is a logical next step to quantify the property characterizing equilibrated overflow, namely product salinity, in different cases. Any change in the probability distribution function of overflow salinity is irreversible, and by definition related to mixing processes. Care is needed regarding two aspects of product salinity computation. First, it is important to consider the structure of the salinity distribution in the overflow plume rather than only the average salinity, for reasons given in Section 1. Second, one has to be cautious how to assess the changes in the product salinity distribution. For instance, product salinity distribution as a function of the geo-potential coordinate is not the best choice in the presence of topographic roughness.

Here, we define a time-mean, span-wise averaged salinity distribution $\bar{S}^k(x_i)$ at sections x_i based on $k = 1, \dots, (N - 1)$ overflow layers with identical average salinities (or equal isohalines),

$$\bar{S}^k(x_i) = \frac{1}{(\tau - \tau_s)L_y} \int_{\tau_s}^{\tau} \int_0^{L_y} \frac{1}{h^k(x_i, y', t')} \int_{z_b(x_i, y')}^H S(x_i, y', z', t') \delta^k(x_i, y', z', t') dz' dy' dt', \quad (12)$$

where z_b is the bottom level, τ_s is the time it takes for the overflow to reach the separation point, h^k is the thickness of the overflow layer defined as

$$h^k(x_i, y, t) \equiv \int_{z_b}^H \delta^k(x_i, y, z', t) dz' \quad \text{where} \quad \delta^k(x_i, y, z, t) = \begin{cases} 1, & \text{when } \epsilon_{k-1} \leq S(x_i, y, z, t) < \epsilon_k \\ 0, & \text{otherwise} \end{cases} \quad (13)$$

where $\epsilon_k = \Delta S(k - 1)/(N - 1)$, and we take $N = 11$ here.

Another important quantity of interest is the overflow mass transport. Here, we define a time-mean mass transport in each isohaline layer k and across section at x_i as

$$\bar{Q}^k(x_i) = \frac{1}{(\tau - \tau_s)L_y} \int_{\tau_s}^{\tau} \int_0^{L_y} \int_{z_b}^H \mathbf{u} \cdot \mathbf{n} \delta^k dz' dy' dt', \quad (14)$$

where \mathbf{n} is the unit vector perpendicular to the section. Since the overflow is defined by the smallest salinity anomaly, its total transport across a section at x_i is given by $Q_o(x_i) = \sum_{k=2}^{N-1} \bar{Q}^k(x_i)$, whereas that of the ambient flow is $Q_a(x_i) = \bar{Q}^1(x_i)$. Because of the boundary condition used in these numerical experiments, $Q_o(x_i) + Q_a(x_i) = 0$.

$\bar{S}^k(x_i)$ and $\bar{Q}^k(x_i)$ are quantified at two locations. First at $x_0 = 1$ km which corresponds to source water properties, and second at $x_1 = x_s + \ell$ to measure the product water properties. A distance of $\ell = 1$ km from the span-wise averaged separation location x_s is found to be far enough for the residual mixing to subside and the effects of topographic roughness on product salinity to become negligible. It is also more revealing to deal with normalized quantities, namely with $\bar{S}^k(x_i)/\Delta S$ versus $\bar{Q}^k(x_i)/Q_o(x_i)$.

Distribution of the salinity classes $\bar{S}^k/\Delta S$ as a function of mass transport \bar{Q}^k/Q_o at the source section x_0 is shown in Fig. 9a in experiments with $R_p = 0.4$ and bottom roughness parameters $a = 0, 0.1, 0.2, 0.4, 0.6$. This figure shows that the overflow entering the system is transported mostly in high salinity classes ($\bar{S}^k/\Delta S \geq 0.6$), due to conditions imposed for the inlet forcing (see Fig. 1 in Özgökmen et al., 2006). The slight loss of transport at the highest salinity class is due to the bottom boundary layer generated by the no-slip boundary condition. The return flow takes place at the lowest salinity class, which corresponds to the ambient flow. Fig. 9a also shows that there is no significant difference between cases with different a . The results shown in Fig. 9a can be distilled further by defining a transport-weighted salinity

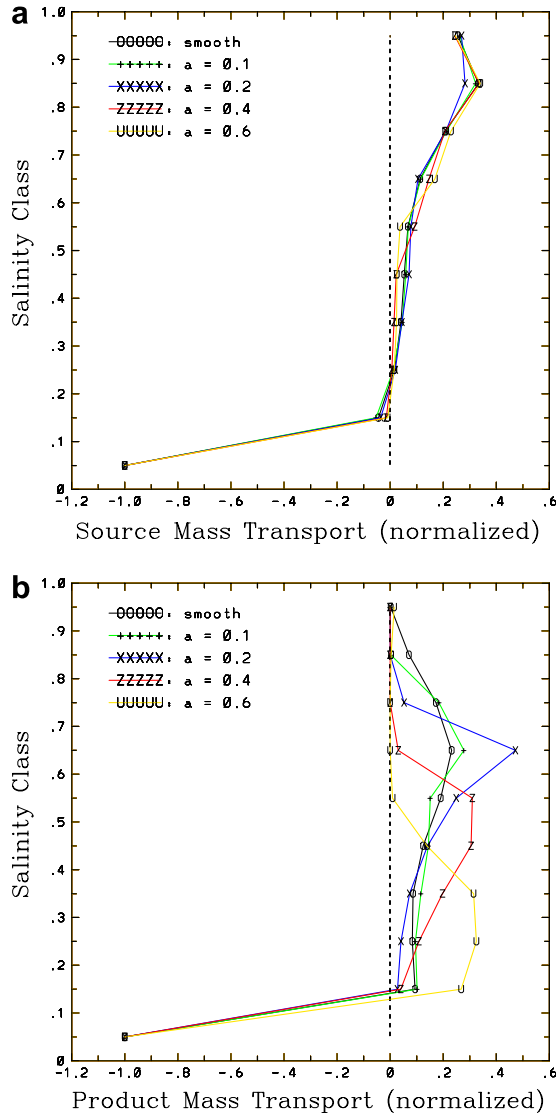


Fig. 9. Salinity classes $k = 1, \dots, 10$ as a function of transport distribution at the locations of (a) source water inflow, $\bar{S}^k(x_0)/\Delta S$ versus $\bar{Q}^k(x_0)/Q_0(x_0)$, and (b) product water equilibration, $\bar{S}^k(x_1)/\Delta S$ versus $\bar{Q}^k(x_1)/Q_0(x_1)$, in experiments with $R_p = 0.4$ and $a = 0, 0.1, 0.2, 0.4, 0.6$.

$$\langle S(x_i) \rangle = \frac{\sum_{k=2}^{N-1} \bar{S}^k(x_i) \bar{Q}^k(x_i)}{Q_0(x_i)}. \tag{15}$$

The transport-weighted salinity of the source water is $S_P/\Delta S = \langle S(x_0) \rangle/\Delta S \approx 0.78$ in all cases. These source distributions provide a reference for the product salinity distribution.

The transport of product waters in different salinity classes is shown in Fig. 9b. First, we note that the product salinity distribution of the overflow over smooth topography is such that while most of the transport now takes place in intermediate classes ($0.4 \leq \frac{\bar{S}^k}{\Delta S} \leq 0.7$), mixing appears to have been unable to dilute dense salinity classes in the range of ($0.8 \leq \frac{\bar{S}^k}{\Delta S} \leq 0.9$). When bottom roughness is introduced with $a = 0.1$ or $a = 0.2$, salinities in the range of $0.8 \leq \frac{\bar{S}^k}{\Delta S} \leq 0.9$ diminish. While the transport-weighted salinities of these three cases ($a = 0, 0.1, 0.2$) are very similar (Table 4), changes in the product salinity distribution and in particular the removal of the high salinity classes make a significant difference regarding the separation from the bottom (Fig. 7). When

the roughness parameter a is increased further, the trend continues. In the case with $a = 0.6$, all of the overflow product transport is confined to $0.1 \leq \frac{S_p}{\Delta S} \leq 0.5$, illustrating the significant effect of bottom roughness on the removal of the highest salinity classes from the overflow product distribution.

It was shown in Özgökmen et al. (2006) that when the ambient stratification parameter R_ρ was increased, the average product water salinity increased as well. This is not only because the overturning scales at the interface between the overflow and the ambient fluid become smaller (which reduces the net entrainment and dilution of the overflow) but also because the distance traveled by the overflow until reaching the equilibrium level is reduced as well, approximately via (10). Distributions of overflow mass transport in product salinity classes from the present experiments are plotted in Fig. 10. Fig. 10a shows how the product salinity distribution changes with R_ρ for smooth bottom ($a = 0$) case, whereas Fig. 10b depicts the same in the case of rough bottom ($a = 0.2$). In both cases, it is quite clear that an increase in R_ρ leads to higher salinity classes in the product overflow. Therefore, regarding the product salinity distributions, increases in bottom roughness and ambient stratification parameters act in the opposing sense. This can be explained in that an increase in bottom roughness induces vertical velocities in the overflow that facilitate the mixing of highly saline bottom waters with other fluid, whereas an increase in R_ρ tends to reduce the vertical excursions of the fluid parcels. Also, the overflow has to travel over a shorter distance with rough topography to reach neutral buoyancy when R_ρ is larger. As such, high salinity classes that are diluted in overflows over rough topography (black lines in Fig. 10a and b) are preserved in the presence of stronger ambient stratification (red line in Fig. 10b).

4.5. Bottom drag

The results depicted thus far inevitably raise the following questions:

- Are there any changes taking place in the structure of the gravity current flowing over rough topography? What are some of the circulation patterns responsible for the significant differences with respect to flows over smooth topography?

To address these questions, representative flow patterns from simulations over smooth and rough topography are shown in Fig. 11. The overflow over smooth topography has a familiar structure in light of the recent concepts put forth by Peters and Johns (2005); it consists of an interfacial layer between the light ambient fluid and dense overflow, and a bottom layer (Fig. 11a). The interfacial layer is characterized by overturns caused by shear instability, occupying approximately half the overflow thickness, as estimated in (1). The bottom layer transports high salinity overflow classes and seems fairly immune from dilution, in part also due to the laminarizing effect of the shear stress in the boundary layer near the solid boundary. The situation is completely different in the case of rough bottom, in which the overflow characterized by separating flows and recirculating eddies in the lee of topographic obstacles (Fig. 11b). While the 3D circulation patterns are far more complex than shown in this 2D snapshot, the insight gained from this figure is adequate to raise the following question:

- What is the drag exerted by the rough topography on the overflow?

In order to answer this question, we define a skin drag coefficient arising from the shearing (tangential) stress at the bottom:

$$C_f(t) \approx \frac{1}{\frac{1}{2}\rho_0 U_0^2 L_y \bar{x}^*(t)} \int_0^{L_y} \int_0^{x^*(y,t)} \rho_0 v_{hr} \left[\left(\frac{\partial u}{\partial z} \right)_{z_b}^2 + \left(\frac{\partial v}{\partial z} \right)_{z_b}^2 \right]^{1/2} dx dy \quad (16)$$

Table 4

Transport weighted product salinity $S_p/\Delta S$ as a function of bottom roughness parameter in experiments a with $R_\rho = 0.4$

$a = 0$	$a = 0.1$	$a = 0.2$	$a = 0.4$	$a = 0.6$
0.52	0.50	0.53	0.38	0.27

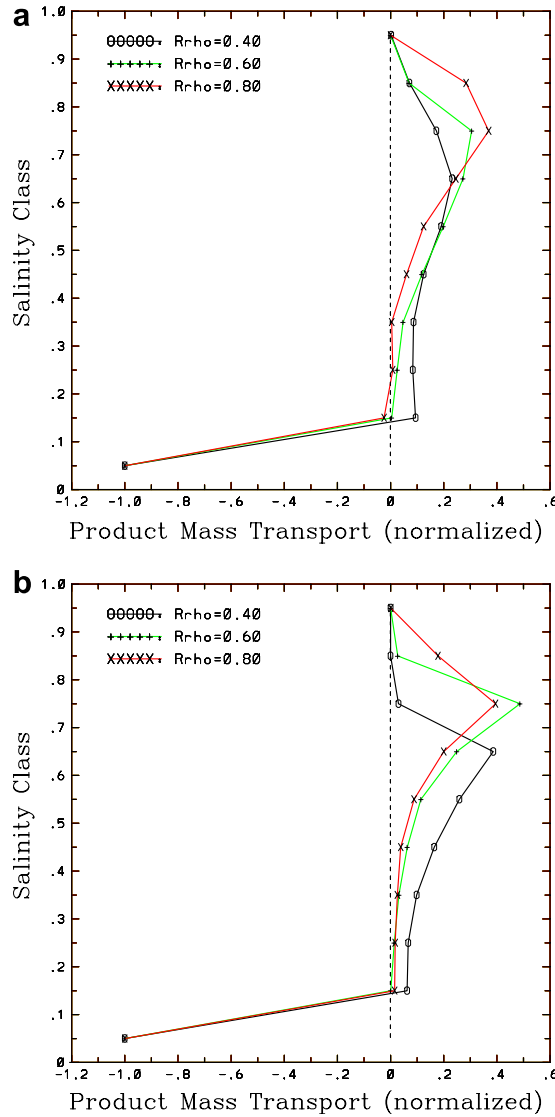


Fig. 10. Overflow mass transport in salinity classes for product waters in the case of: (a) smooth topography ($a = 0$), and (b) rough topography with $a = 0.2$, by varying ambient stratification parameter $R_{\rho} = 0.4; 0.6; 0.8$.

where $U_0 = \sqrt{g'h_0}$ is the overflow speed scale and $x^*(y, t) = \min[X_F(y, t), x_{\max}(y, t)]$ is the length of the overflow in direct contact with topography.

The separation of the gravity current flow in the lee of the topographic crests implies a drop in pressure, giving rise to normal forces, thus so-called pressure or form drag. The form drag coefficient in the stream-wise direction is defined as:

$$C_p^x(t) = \frac{1}{\frac{1}{2}\rho_0 U_0^2 L_y \overline{x^*}(t)} \int_0^{L_y} \int_0^{x^*(y,t)} p_{z_b} \frac{\partial \eta}{\partial x} dx dy, \tag{17}$$

where p_{z_b} is the bottom pressure. Several comments need to be made about Eq. (17). First, the difference between x -direction and the direction along the background slope is ignored because $\cos \theta \approx 0.9986$. Second, the concept of form drag is most meaningful for flows around isolated objects (Pratt and Whitehead, 2007). Eq. (17) is related to the net pressure force acting on the overflow in contact with the bottom, and is referred to as the form drag here.

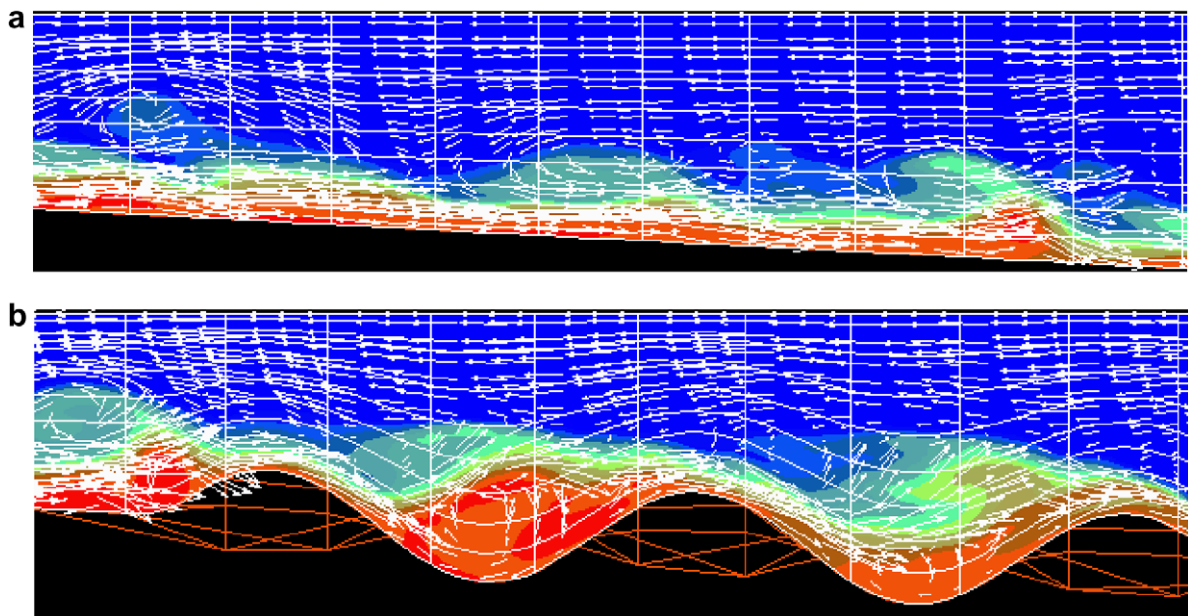


Fig. 11. Snapshots of the salinity and velocity distributions along a streamwise section at $y = 0$ for cases with $R_\rho = 0.4$ and (a) $a = 0$ and (b) $a = 0.2$. (The maximum velocity vector has a magnitude of about 1.2 m s^{-1} .)

The time evolution of skin drag coefficients $C_f(t)$ in the smooth topography case ($a = 0$) is illustrated in Fig. 12a. In the case with the weakest ambient stratification $R_\rho = 0.34$, the skin drag coefficient remains within the range of $2.5 \times 10^{-3} \leq C_f \leq 3 \times 10^{-3}$. Estimates of the skin drag coefficient from overflow observations indicate a broad range of $10^{-3} \leq C_f \leq 10^{-2}$ (Girton and Sanford, 2003; Peters and Johns, 2006). The skin drag coefficient in the present experiments shows a weak dependence on the ambient stratification in that C_f reduces by about 15% when R_ρ increases from 0.34 to 0.80. This is because of the slower propagation speed (11), and reduced shear at the bottom.

The form drag coefficients C_p^x with $R_\rho = 0.4$ are shown in Fig. 12b. The leveling off of the drag coefficients occurs after the separation of the plume from the slope (Table 3). The main point of this figure is that the form drag coefficients for $a = 0.1$ is nearly twice as large as C_f , about 10 times as large for $a = 0.2$ and more than 20 times as large for $a = 0.4$ (Fig. 12b, for $R_\rho = 0.4$). The variation in form drag with ambient stratification parameter in the case of constant roughness parameter $a = 0.2$ is also explored. Fig. 12c illustrates that C_p^x doubles when R_ρ is increased from 0.34 to 0.8. The reason for such sensitivity is that the vertical excursions of the water parcels is reduced, and parcels are forced to go around rather than over the obstacles. This tends to enhance leeward flow separation, as recognized from laboratory experiments of stratified flows past spheres (Davies, 1972) and capes (Boyer and Tao, 1987). As such, the form drag coefficient increases with R_ρ .

Clearly, bottom roughness not only leads to enhanced mixing of the tracer fields in overflows, but also imparts significantly enhanced drag on the velocity field as well.

4.6. Overflow mass transport

Observations of the few main overflows in the ocean indicate that not only the property distributions of the product water masses but also their mass transport is usually modified, by entrainment of ambient water (Price and Baringer, 1994). In light of the results above, it is necessary to ask the following question:

- How is the overflow mass transport influenced by the topographic roughness?

To address this question, it is useful to start from a traditional idealized example (Price and Baringer, 1994). Consider a parcel of fluid of height \mathcal{H} that is denser than the ambient fluid density of ρ_0 by $\delta\rho$. The parcel is

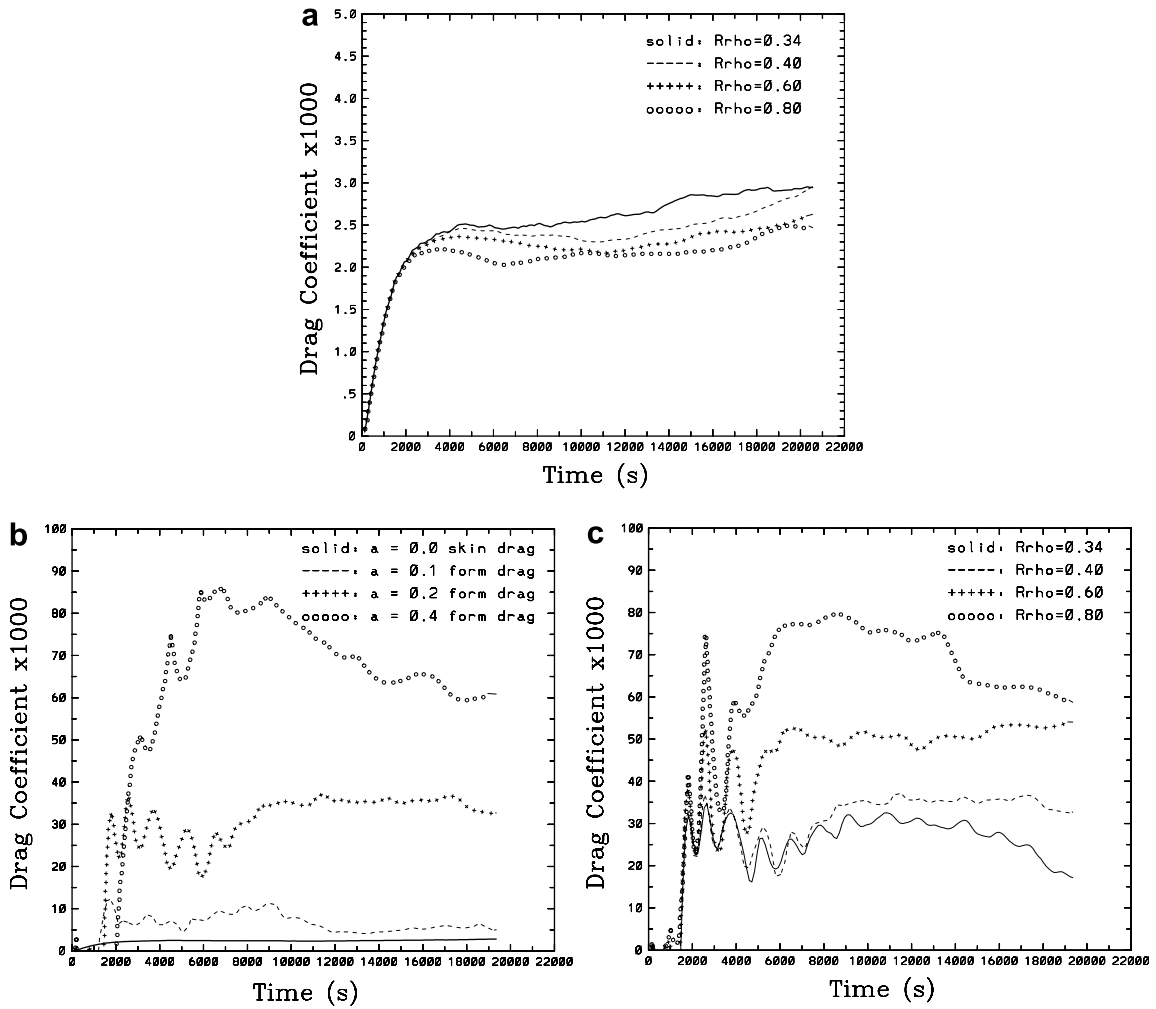


Fig. 12. Comparisons of drag coefficients. (a) Skin drag $C_f(t)$ in the smooth case ($a = 0$) for varying ambient stratification parameter $R_\rho = 0.34; 0.4; 0.6; 0.8$. (b) Comparison of skin drag $C_f(t)$ in the smooth case ($a = 0$) to form drag $C_p^x(t)$ in cases with rough topography ($a = 0.1; 0.2; 0.4$) for constant ambient stratification parameter $R_\rho = 0.4$. (c) Variation of form drag $C_p^x(t)$ as a function of the ambient stratification parameter $R_\rho = 0.34; 0.4; 0.6; 0.8$ for constant roughness parameter $a = 0.2$.

on a wedge with slope angle θ from the horizontal. The conservation of momentum in the along slope direction x can be written as:

$$\rho_0 \frac{dU}{dt} = -\frac{\partial p}{\partial x} + g\delta\rho \sin\theta - \frac{\tau_b}{\mathcal{H}} - \frac{\tau_e}{\mathcal{H}}, \tag{18}$$

where τ_b is the bottom stress and τ_e represents the stress imparted on the water parcel due to entrainment of stagnant ambient fluid. Assuming that the pressure gradient forces are negligible in the steady state, and that the bottom stress can be parameterized via $\tau_b \approx \frac{1}{2}\rho_0 U^2 C_d$ and entrainment stress by $\tau_e \approx \rho_0 w_E U$ with w_E being the net entrainment velocity, Eq. (18) can be rewritten as

$$\frac{g'\mathcal{H}}{U^2} \sin\theta = \frac{C_d}{2} + \frac{w_E}{U}, \tag{19}$$

where $g' = g\delta\rho/\rho_0$ is the local reduced gravity. By recognizing the local Froude number $Fr = U/\sqrt{g'\mathcal{H}}$, the entrainment parameter $E = w_E/U$ can be expressed as

$$E = Fr^{-2} \sin \theta - \frac{C_d}{2}. \quad (20)$$

We assume that most of the entrainment takes place when the gravity currents are near critical, namely $Fr \approx 1$. If it is also assumed that the topography is smooth, slope angle is small and the Reynolds number is high enough to result in small C_d , then Eq. (20) implies that $E \sim \theta$ provides a simple relationship for the entrainment parameter, as pursued in laboratory (Turner, 1986) and numerical experiments (Özgökmen et al., 2003). Eq. (20) indicates also that bottom drag can influence the entrainment parameter. In particular, $E = 0$ when $C_d = 2 \sin \theta$ (and $Fr = 1$). Using the background slope of $\theta = 3^\circ$, the limiting drag coefficient becomes $C_d = 100 \times 10^{-3}$, which is within the range of form drag coefficients estimated for some cases here (Fig. 12b and c). As such, one would expect a significant decrease in the entrainment parameter in those cases with high a and R_ρ . Physically, this implies that the gravitational acceleration is entirely balanced by bottom drag.

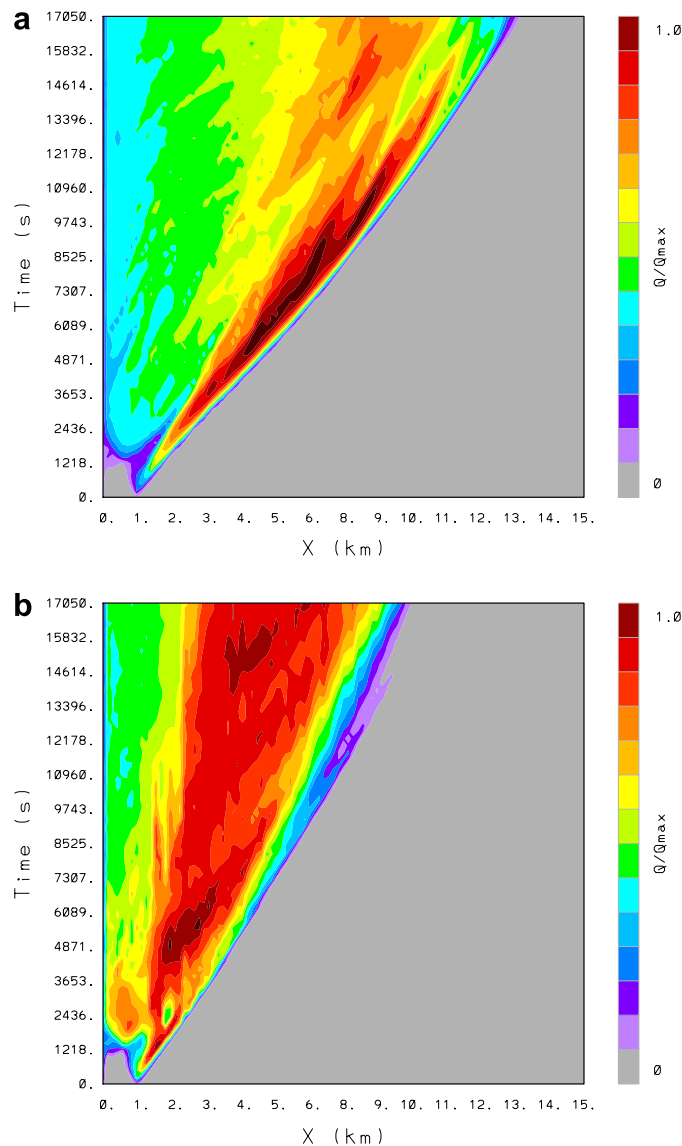


Fig. 13. Hovmoeller diagrams of the overflow mass transport $Q_0(x,t)$ normalized by the maximum transport in experiments with: (a) smooth topography, and (b) rough topography ($a = 0.4$). The ambient stratification parameter is $R_\rho = 0.40$ in both cases.

But, one of the important short comings of Eq. (20) is that the Lagrangian evolution of the water parcel is neglected, namely it is not revealing about the space and time dependence of entrainment in the overflow. Second, it is known that topographic perturbations can enhance entrainment by facilitating vertical motions and overturning (Özgökmen et al., 2004a), as well as causing internal waves. But these complex processes are not well understood and not included in (20). Thus, it seems that bottom roughness can lead to two seemingly competing effects; it can act to enhance both the entrainment and bottom drag. It is not clear a-priori which effect would dominate here.

In order to quantify entrainment from the numerical experiments, it is equally effective to compute its integrated effect, namely changes in the overflow mass transport. The overflow transport $Q_o(x, t)$ (normalized by its maximum value) is plotted in selected experiments over smooth and rough topography in Fig. 13. In the case of smooth topography (Fig. 13a), the high Q_o trailing the propagation line is associated with the head vortex (Fig. 3a). In the trailing overflow, the increase in mass transport occurs gradually over the slope

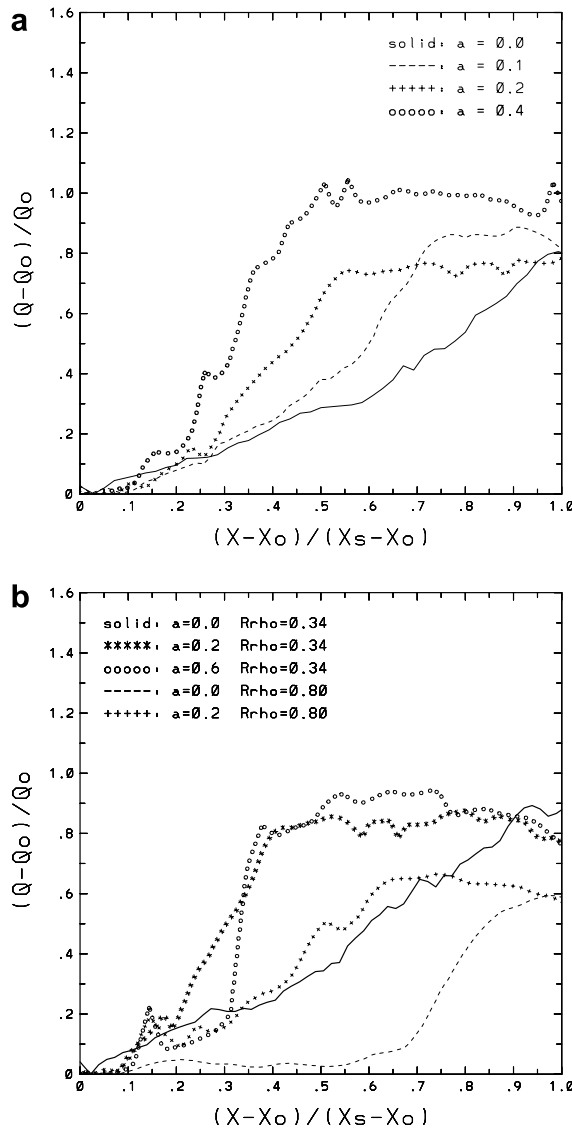


Fig. 14. Overflow mass transport with downstream distance, $Q_o^*(x^*)$: (a) in experiments with increasing bottom roughness parameter but constant ambient stratification parameter $R_p = 0.40$, and (b) in experiments in which both the bottom roughness and ambient stratification parameters change.

and the maximum transport is located at $x = 8$ to $x = 9$ km, near the separation point. In contrast, in the rough topography case (Fig. 13b), most of the mass transport increase takes place over a very short distance between $x = 1$ and $x = 3$ km. Then it remains approximately constant, which indicates that no further entrainment takes place. Thus, entrainment appears to be distributed over the whole slope in the smooth bottom case, while it is limited to the top of the slope in the rough bottom case. Therefore, it seems that topographic perturbations act to enhance entrainment at the top of the slope, but then high drag develops downstream and terminates further entrainment. A striking observation is that in both cases, the net transport appears to increase by the same ratio with respect to the inflow.

In order to quantify the differences in mass transport change in various experiments, the non-dimensionalized mean mass transport, $Q_o^*(x^*) = (\overline{Q_o}(x^*) - \overline{Q_o}(0)) / \overline{Q_o}(0)$, is plotted as a function of non-dimensionalized downstream distance $x^* = (x - x_0) / (x_s - x_0)$. Here, the overbar indicates time averaging (during the period of $13,000 \leq t \leq 17,000$ based on Fig. 13), the subscript indicates the inlet at $x = x_0$ (taken as $x_0 = 1$ km), x_s is the separation point from the bottom in each experiment. $Q_o^*(x^*)$ is plotted in Fig. 14a in experiments with increasing bottom roughness parameter, $a = 0; 0.1; 0.2; 0.4$, and constant $R_\rho = 0.40$. The mass transport of the overflow released into the interior at the separation point is within a narrow range of $0.8 \leq Q_o^*(1) \leq 1$, corresponding approximately to a doubling of the source transport. The main difference between cases depicted in Fig. 14a is that as the roughness parameter a is increased, entrainment starts over a shorter distance down the slope and also stops over a shorter distance as well. In order to explore whether this surprising pattern persists in experiments with other R_ρ , $Q^*(x^*)$ is plotted in experiments in which both the bottom roughness and ambient stratification parameters change (Fig. 14b). Again, $Q_o^*(1)$ is found to be not very sensitive to a , but it is mainly a function of R_ρ ; $Q_o^*(1)$ decreases with R_ρ , as pointed out before based on experiments over smooth bottom topography by Özgökmen et al. (2006).

5. Summary and conclusions

Overflows play a critical role in deep-water formation in the ocean. Therefore, it is thought that they carry importance for the oceanic thermohaline circulation, with possible implications for climate dynamics as well. The present study is motivated by two recent conceptual developments. The first is that some overflows have been shown to have a vertical density structure (Peters and Johns, 2005). The second is that some overflows are shown to be influenced by details of bottom topography (Chang et al., in press; Riemenschneider and Legg, 2007; Ezer, 2006). Here, we try to address the question of whether and how bottom roughness modifies the vertical density structure of overflows.

To this end, numerical simulations of bottom gravity currents are conducted in the presence of ambient stratification, for cases in which equilibrated product water masses are formed. The computations are based on 3D non-hydrostatic spectral element model Nek5000, which combines the geometrical flexibility of the finite element method with the numerical accuracy of the spectral method. Both model capabilities are of critical importance in this study. The numerical domain consists of a wedge with a background slope of $\theta = 3^\circ$. Sinusoidal perturbations are superimposed on this background topography as a simple representation of bottom roughness. The overflow is represented by a salinity anomaly entering the domain at the top of the wedge. The ambient fluid is stratified with a linear temperature profile. This setup allows for a convenient identification of the overflow water masses after neutral equilibrium is achieved. The main experimental matrix consists of the bottom roughness parameter and the strength of the ambient stratification.

The main finding of the present study is that bottom roughness can significantly modify the distribution of salinity classes in the overflow product by removing the transport barrier between so-called bottom layer (transporting densest overflow water) and interfacial layer (to which most of the entrainment is confined). This happens by flow separation and recirculating eddies forming in the lee of topographic barriers. As a result, overflow product water masses lack the high salinity classes that determine the separation level in the ambient fluid. As such, the buoyancy equilibrium takes place higher up in the water column.

While the impact of bottom roughness on overflow product salinity distribution is a relatively intuitive result, this study has two surprising findings. The first is that we quantified the form drag coefficient after noticing flow separation in the lee of rough bottom elements. It is found that the form drag coefficients over rough topography can be an order of magnitude larger than the skin drag coefficient over smooth topography.

To our knowledge, form drag has never been quantified in oceanic overflows since this requires high-resolution (probably both in space and time) pressure measurements in the vicinity of rough topography. This appears to be an expensive and technically challenging task, if one is to achieve a synoptic data set. Nevertheless, the possible role of form drag on overflows has already been put forth (Peters and Johns, 2006). High form drag also leads to a sluggish propagation, consistent with previous results (Özgökmen et al., 2004a; Chang et al., in press; Riemenschneider and Legg, 2007). These results imply that it should be considered to enhance both the eddy diffusivity (via terms in the tracer conservation equation) and bottom drag (via terms in the momentum conservation equations) according to fine-scale bottom roughness on the path of various overflows in realistic oceanic simulations.

The second surprising outcome is that the ratio of the change of the overflow transport with respect to the inflow transport is found to be surprisingly robust to changes in the bottom roughness parameter. While overflow transport increases gradually over the slope in the case of smooth topography, the entrainment gets enhanced, but becomes gradually restricted to take place over shorter distances at the top of the slope, as bottom roughness parameter is increased. Further down the slope, entrainment shuts off due to development of high drag. Apparently, the integrated effect of these phenomena lead to similar outcomes. Nevertheless, it seems unlikely that this can be a universal result for all types of topographies. As such, further work is needed with different shapes of topographic roughness to explore this issue in more detail. We could not help notice that an approximately doubling of overflow mass transport (quite robust result in the present simulations over the range of R_ρ) between the source and product regions is a fairly common estimate for many oceanic overflows (e.g., table of overflow observations available from http://cpt-gce.org/Table_of_observations.htm).

We conclude that fine-scale details of topography matter not only for the main overflow pathways (Chang et al., in press) but also regarding the product water distribution. As such, development of accurate parameterizations of overflows for climate simulations remains a challenging task.

Acknowledgements

We greatly appreciate the support of National Science Foundation via grants OCE 0336799, OCE 0326648, OCE 0620661, and the Mathematical, Information, and Computational Sciences Division subprogram of the Office of Advanced Scientific Computing Research, US Department of Energy, under Contract W-31-109-ENG-38. We thank Hartmut Peters and Marcello Magaldi for their time spent reading this manuscript and many helpful comments. We also thank the two anonymous reviewers for their constructive comments, which helped improve the manuscript.

References

- Andreassen, O., Hvidsten, P.O., Fritts, D.C., Arendt, S., 1998. Vorticity dynamics in a breaking internal gravity wave. part 1. initial instability evolution. *J. Fluid Mech.* 367, 27–46.
- Baines, P.G., 2001. Mixing in flows down gentle slopes into stratified environments. *J. Fluid Mech.* 443, 237–270.
- Baines, P.G., 2002. Two-dimensional plumes in stratified environments. *J. Fluid Mech.* 471, 315–337.
- Baines, P.G., 2005. Regimes for the flow of dense fluid down slopes into stratified environments. *J. Fluid Mech.* 538, 245–267.
- Baringer, M.O., Price, J.F., 1997. Mixing and spreading of the Mediterranean outflow. *J. Phys. Oceanogr.* 27, 1654–1677.
- Benjamin, T., 1968. Gravity currents and related phenomena. *J. Fluid Mech.* 31, 209–248.
- Bloomfield, L., Kerr, R., 1998. Turbulent fountains in a stratified fluid. *J. Fluid Mech.* 358, 335–356.
- Boyer, D., Tao, L., 1987. On the motion of linearly stratified rotating fluids past capes. *J. Fluid Mech.* 180, 429–449.
- Britter, R., Linden, P., 1980. The motion of the front of a gravity current traveling down an incline. *J. Fluid Mech.* 99, 531–543.
- Cenedese, C., Whitehead, J.A., Ascarelli, T.A., Ohiwa, M., 2004. A dense current flowing down a sloping bottom in a rotating fluid. *J. Phys. Oceanogr.* 34, 188–203.
- Chang, Y., Özgökmen, T., Peters, H., Xu, X., in press. Numerical simulation of the Red Sea outflow using HYCOM and comparison with REDSOX observations. *J. Phys. Oceanogr.*
- Chang, Y., Xu, X., Özgökmen, T., Chassignet, E., Peters, H., Fischer, P., 2005. Comparison of gravity current mixing parameterizations and calibration using a high-resolution 3d nonhydrostatic spectral element model. *Ocean Modell.* 10, 342–368.
- Davies, P., 1972. Experiments on Taylor columns in rotating stratified fluids. *J. Fluid Mech.* 54, 691–717.
- Dryja, M., Widlund, O.B., 1987. An additive variant of the Schwarz alternating method for the case of many subregions. Technical Report 339, Dept. Computer Science, Courant Institute.

- Ellison, T.H., Turner, J.S., 1959. Turbulent entrainment in stratified flows. *J. Fluid Mech.* 6, 423–448.
- Ezer, T., 2005. Entrainment, diapycnal mixing and transport in three-dimensional bottom gravity current simulations using the Mellor–Yamada turbulence scheme. *Ocean Modell.* 9, 151–168.
- Ezer, T., 2006. Topographic influence on overflow dynamics: idealized numerical simulations and faroe bank channel overflow. *J. Geophys. Res. Oceans* 111. doi:10.1029/2005JC003195.
- Ferron, B., Mercier, H., Speer, K., Gargett, A., Poltzin, K., 1998. Mixing in the romanche fracture zone. *J. Phys. Oceanogr.* 28, 1929–1945.
- Fischer, P., 1997a. An overlapping Schwarz method for spectral element solution of the incompressible Navier–Stokes equations. *J. Comp. Phys.* 133, 84–101.
- Fischer, P., Gottlieb, D., 1997. On the optimal number of subdomains for hyperbolic problems on parallel computers. *Int. J. Supercomp. Appl. High Perf. Comp.* 11, 65–76.
- Fischer, P., Mullen, J., 2001. Filter-based stabilization of spectral element methods. *C.R. Acad. Sci. Paris Sér. I Math.*, 0764-4442 332 (3), 265–270.
- Fischer, P.F., 1997b. An overlapping schwarz method for spectral element solution of the incompressible Navier–Stokes equations. *J. Comput. Phys.* 133 (1), 84–101.
- Fischer, P.F., Ronquist, E.M., 1994. Spectral element methods for large scale parallel Navier–Stokes calculation. *Comput. Meth. Appl. Mech. Eng.* 116, 69.
- Fritts, D.C., Arendt, S., Andreassen, O., 1998. Vorticity dynamics in a breaking internal gravity wave. part 2. vortex interactions and transition to turbulence. *J. Fluid Mech.* 367, 47–65.
- Gargett, A., 1994. Observing turbulence with a modified acoustic doppler profiler. *J. Atmos. Ocean. Tech.* 11, 1592–1610.
- Gargett, A., Osborn, T., Nasmyth, P., 1984. Local isotropy and the decay of turbulence in a stratified fluid. *J. Fluid Mech.* 144, 231–280.
- Gibson, C., Nabatov, V., Ozmidov, R., 1993. Measurements of turbulence and fussy turbulence near Ampere seamount. *Dyn. Atmos. Oceans* 19, 175–204.
- Girton, J.B., Sanford, T.B., 2003. Descent and modification of the overflow plume in the Denmark Strait. *J. Phys. Oceanogr.* 33, 1351–1363.
- Girton, J.B., Sanford, T.B., Käse, R.H., 2001. Synoptic sections of the Denmark Strait overflow. *Geophys. Res. Lett.* 28, 1619–1622.
- Gordon, A., Zambianchi, E., Orsi, A., Visbeck, M., Giulivi, C., Whitworth III, T., Spezie, G., 2004. Energetic plumes over the western Ross Sea continental slope. *Geophys. Res. Lett.* 31 (L21302).
- Hallworth, M., Huppert, H., Philips, J., Spark, S., 1996. Entrainment in two-dimensional and axisymmetric turbulent gravity current. *J. Fluid Mech.* 308, 289–311.
- Keulegan, G.H., 1958. The motion of saline fronts in still water. Technical Report 339, US Nat. Bur. Stand.
- Killworth, P., 1977. Mixing on the weddell sea continental slope. *Deep-Sea Res.* 24, 427–448.
- Klaassen, G.P., Peltier, W.R., 1989. The role of transverse secondary instabilities in the evolution of free shear layers. *J. Fluid Mech.* 202, 367–402.
- Klaassen, G.P., Peltier, W.R., 1991. The influence of stratification on secondary instability in free shear layers. *J. Fluid Mech.* 227, 71–106.
- Kunze, E., Toole, J., 1997. Tidally driven vorticity, diurnal shear, and turbulence atop fieber-ling seamount. *J. Phys. Oceanogr.* 27, 2663–2693.
- Lavelle, J., Lozovatsky, I., Smith, D., 2004. Tidally induced turbulent mixing at Irving Seamount – modeling and measurements. *Geophys. Res. Lett.* 31 (L10308). doi:10.1029/2004GL019706.
- Ledwell, J., Montgomery, E., Polzin, K., Laurent, a.R.S.L.C.St., Toole, J., 2000. Evidence for enhanced mixing over rough topography in the abyssal ocean. *Nature* 403, 179–182.
- Legg, S., Hallberg, R.W., Girton, J.B., 2006. Comparison of entrainment in overflows simulated by z-coordinate, isopycnal and non-hydrostatic models. *Ocean Modell.* 11, 69–97.
- Lesieur, M., 1997. *Turbulence in Fluids*. In: *Fluid Mechanics and its Applications*, vol. 40. Kluwer Academic Publishers.
- Lottes, J.W., Fischer, P.F., 2005. Hybrid multigrid/schwarz algorithms for the spectral element method. *J. Sci. Comput.* 24 (1), 45–78.
- Lueck, R., Mudge, T., 1997. Topographically induced mixing around a shallow seamount. *Science* 276, 1831–1833.
- Maday, Y., Patera, A.T., 1989. Spectral element methods for the Navier–Stokes equations. In: Noor, A.K. (Ed.), *State of the Art Surveys in Computational Mechanics*. ASME, pp. 71–143.
- Maday, Y., Patera, A.T., Ronquist, E.M., 1990. An operator-integration-factor splitting method for time-dependent problems: applications to incompressible fluid flow. *J. Sci. Comput.* 5 (4), 263–292.
- Marshall, J., Schott, F., 1999. Open-ocean convection: observations, theory, and models. *Rev. Geophys.* 37, 1–64.
- Moum, J., 1996. Energy containing scales of turbulence in the ocean thermocline. *J. Geophys. Res. Oceans* 101 (C6), 14085–14109.
- Moum, J., Caldwell, D., Nash, J., Gunderson, G., 2002. Observations of boundary mixing over the continental slope. *J. Phys. Oceanogr.* 32, 2113–2130.
- Munk, W., Wunsch, C., 1998. Abyssal recipes ii: energetics of tidal and wind mixing. *Deep Sea Res. I* 45, 1977–2010.
- Nabatov, V., Ozmidov, R., 1988. A study of turbulence over underwater mountains in the Atlantic Ocean (in Russian). *Oceanology* 28, 210–217.
- Özgökmen, T., Fischer, P., Johns, W., 2006. Product water mass formation by turbulent density currents from a high-order nonhydrostatic spectral element model. *Ocean Modell.* 12, 237–267.
- Özgökmen, T., Iliescu, T., Fischer, P., Srinivasan, A., Duan, J., 2007. Large eddy simulation of stratified mixing in two-dimensional dam-break problem in a rectangular enclosed domain. *Ocean Modell.* 16, 106–140.

- Özgökmen, T.M., Chassignet, E.P., 2002. Dynamics of two-dimensional turbulent bottom gravity currents. *J. Phys. Oceanogr.* 32, 1460–1478.
- Özgökmen, T.M., Fischer, P.F., Duan, J., Iliescu, T., 2004a. Entrainment in bottom gravity currents over complex topography from three-dimensional nonhydrostatic simulations. *Geophys. Res. Lett.* 31 (L13212). doi:10.1029/2004GL020186.
- Özgökmen, T.M., Fischer, P.F., Duan, J., Iliescu, T., 2004b. Three-dimensional turbulent bottom density currents from a high-order nonhydrostatic spectral element model. *J. Phys. Oceanogr.* 34 (9), 2006–2026.
- Özgökmen, T.M., Johns, W., Peters, H., Matt, S., 2003. Turbulent mixing in the Red Sea outflow plume from a high-resolution nonhydrostatic model. *J. Phys. Oceanogr.* 33, 1846–1869.
- Patera, A.A., 1984. spectral element method for fluid dynamics; laminar flow in a channel expansion. *J. Comp. Phys.* 54, 468–488.
- Peters, H., Johns, W.E., 2005. Mixing and entrainment in the Red Sea outflow plume. ii. turbulence characteristics. *J. Phys. Oceanogr.* 35, 584–600.
- Peters, H., Johns, W.E., 2006. Bottom layer turbulence in the red sea outflow plume. *J. Phys. Oceanogr.* 36, 1763–1785.
- Peters, H., Johns, W.E., Bower, A.S., Fratantoni, D.M., 2005. Mixing and entrainment in the Red Sea outflow plume. i. plume structure. *J. Phys. Oceanogr.* 35, 569–583.
- Poltzin, K., Toole, J., Ledwell, J., Schmitt, R., 1997. Spatial variability of turbulent mixing in the abyssal ocean. *Science* 276, 93–96.
- Pope, S., 2000. *Turbulent Flows*. Cambridge University Press, Cambridge, ISBN 0-521-59886-9.
- Pratt, L., Whitehead, J., 2007. In: *Atmospheric and Oceanographic Sciences Library*, vol. 36. Springer.
- Price, J.F., Baringer, M.O., 1994. Outflows and deep water production by marginal seas. *Prog. Oceanogr.* 33, 161–200.
- Riemenschneider, U., Legg, S., 2007. Regional simulations of the faroe bank channel overflow in a level model. *Ocean Modell.* (17/2), 93–122.
- Schmitz, W., 1995. On the interbasin-scale thermohaline circulation. *Rev. Geophys.* 33, 151–173.
- Simpson, J.E., 1987. *Gravity Currents in the Environment and the Laboratory*. John Wiley and Sons, New York.
- Smith, P., 1975. A streamtube model for bottom boundary currents in the ocean. *Deep-Sea Res.* 22, 853–873.
- Spall, M., Pickard, R., 2001. Where does dense water sink? *J. Phys. Oceanogr.* 31, 143–173.
- Taylor, G., 1935. Statistical theory of turbulence. *Proc. R. Soc. London A* 151, 421–454.
- Thurnherr, A., 2006. Diapycnal mixing associated with an overflow in a deep submarine canyon. *Deep-Sea Res. II* 53, 194–206.
- Thurnherr, A., Laurent, L.S., Speer, K., Toole, J., Ledwell, J., 2004. Mixing associated with sills in a canyon on the mid-ocean ridge flank. *J. Phys. Oceanogr.* 35, 1370–1381.
- Thurnherr, A., Speer, K., 2003. Boundary mixing and topographic blocking on the Mid-Atlantic Ridge in the South Atlantic. *J. Phys. Oceanogr.* 33, 848–862.
- Tufo, H.M., Fischer, P., 2001. Fast parallel direct solvers for coarse grid problems. *J. Parallel. Distr. Comput.* 173, 431–471.
- Turner, J., 1986. Turbulent entrainment: the development of the entrainment assumption and its application to geophysical flows. *J. Fluid Mech.* 173, 431–471.
- Warren, B., 1981. *Evolution of Physical Oceanography*. In: *Scientific Survey in Honor of Henry Stommel*. MIT Press.
- Weissel, J., Pratson, L., Malinverno, A., 1994. The length-scaling properties of topography. *J. Geophys. Res.* 99, 13997–14012.
- Wunsch, C., Ferrari, R., 2004. Vertical mixing, energy, and the general circulation of the oceans. *Annu. Rev. Fluid Mech.* 36, 281–314.
- Xu, X., Chang, Y., Peters, H., Özgökmen, T., Chassignet, E., 2006. Parameterization of gravity current entrainment for ocean circulation models using a high-order 3d nonhydrostatic spectral element model. *Ocean Modell.* 14, 19–44.
- Xu, X., Chassignet, E., Price, J., Özgökmen, T., Peters, H., in press. A regional modeling study of the entraining mediterranean outflow. *J. Geophys. Res. Oceans*.